Regular Paper

A novel two-layer composite geomembrane lining structure to mitigate frost damage in cold-region canals: Model test and numerical simulation

Haoyuan Jiang [a,b], Mingyi Zhang [a,b,*], Zhengzhong Wang [c], Yi Wang [d], Zhengyi Wang [e], Xinjian Sun [f]

[a] *Key Laboratory of Cryospheric Science and Frozen Soil Engineering, Northwest Institute of Eco-Environment and Resources, Chinese Academy of Sciences, Lanzhou, 730000, China*
[b] *University of Chinese Academy of Sciences, Beijing, 100049, China*
[c] *College of Water Resources and Architectural Engineering, Northwest A&F University, Yangling, 712100, China*
[d] *Nanjing Hydraulic Research Institute, Nanjing, 210024, China*
[e] *College of Civil Engineering and Mechanics, Lanzhou University, Lanzhou, 730000, China*
[f] *College of Civil Engineering and Water Resources, Qinghai University, Xining, 810000, China*

ARTICLE INFO

ABSTRACT

The canal is crucial for water diversion projects, but it is susceptible to frost damage. To address this, a two-layer composite geomembrane lining structure (TLCGLS) was proposed that regulates the interaction between canal lining and frozen soil. Model tests were conducted to investigate its anti-frost heave effectiveness. Considering the interaction among the lining, two-layer composite geomembranes (TLCGs), and frozen soil, a canal frost heave model with heat-water-mechanical coupling was developed. The influence of canal cross-section shapes and TLCGs arrangements on anti-frost heave performance and mechanism of TLCGLS were discussed. Results show that TLCGLS reduces uneven frost heave degree and compressive/tensile strains of the lining by 35%, 29%, and 28% respectively. During melting, it rapidly reduces frost heave, tangential deformation, and strain with minimal residual effects. TLCGLS demonstrates strong resetting ability and excellent anti-frost heave performance. It is particular suitable for arc-bottomed trapezoidal canals. However, excessive reduction in friction between TLCGs weakens arching effect of the bottom lining, increasing tensile stress and safety risks. TLCGLS with geomembrane-geotextile contact exhibits superior anti-frost heave performance, mitigating compressive stress by over 50% while meeting design requirements for tensile stress. These findings provide a theoretical basis and technical solution for mitigating frost damage in canals.

1. Introduction

Water scarcity has been identified as one of the top five global risks, with its impact extending far beyond the social, economic, and environmental challenges that affect people's livelihoods and well-being (World Economic Forum, 2020). In China, the arid and semi-arid regions encompass approximately 47% of the land area (Guo and Shen, 2016), with agricultural irrigation accounting for more than 85% of total regional water consumption (Mao et al., 2018). These regions encounter severe challenges in agricultural, industrial, urban, and ecological water utilization (FAO, 2021). As a result, a range of environmental issues arise including vegetation mortality, decline in

groundwater table, deterioration of water quality, and soil desertification (Berdugo et al., 2020; Scanlon et al., 2023; Haj-Amor et al., 2022). These issues pose risks to national water security, food security, and ecological integrity.

Constructing long-distance water diversion projects and irrigation districts serves as a crucial strategy to alleviate water scarcity and enhance water supply security in arid and semi-arid regions (Faúndez et al., 2023; Gao et al., 2022). However, these regions are mainly located in northwestern China, aligning with the seasonally frozen regions. The harsh environmental conditions characterized by sub-zero temperatures and freeze-thaw cycles result in severe frost damage to water conservancy projects (Jiang et al., 2022a; Li et al., 2024; Liu and Zheng, 2023;

Yu et al., 2020). Canals have emerged as the primary water conveyance structures due to their advantages of simplified construction, convenient maintenance, and cost-effectiveness. However, they are fully exposed to harsh environment, which, combined with an elevated groundwater table resulting from water leakage, leads to severe frost damage (Fig. 1; Hao et al., 2023; Li et al., 2022). This issue significantly contributes to substantial water losses, ranging from approximately 30%–60% of the conveyed volume, necessitating costly annual shutdowns for repairs that severely impact the project's operational safety and efficiency. Therefore, urgent research on frost damage in water conveyance canals is imperative for enhancing water resource utilization.

The harsh environmental and operational conditions contribute to significant heat-water-mechanical coupling phenomena within canals (Fig. 1a), leading to intricate mechanisms of frost damage. Through field and laboratory experiments, the temperature, water content, deformation, and cracks of canals during freezing-thawing have been investigated (Wang et al., 2019; Wang et al., 2024; Zhang and Kushwaha, 1998; Zhu et al., 2021). The identified primary factors causing frost damage include low air temperature, canal water leakage, and frost-susceptible soils (Fig. 1a). To mitigate the impacts of these factors, a series of passive measures for modifying site conditions to prevent frost heave have been proposed. These measures include insulating with insulation boards (Liu et al., 2021; Shao et al., 2023), employing composite geomembranes for anti-seepage (Heibaum, 2014; Tian et al., 2019), installing drainage pipes and digging wells for water discharge (Chen et al., 2023), as well as using gravel to replace frost-susceptible soil (Liu and Zheng, 2023). Remarkable results have been achieved in the preliminary stage. However, the implementation costs of these measures are high, and prolonged foundation burial can cause aging issues, reducing durability and increasing the risk of failure. For instance, extended wet-dry and freeze-thaw cycles causes degradation of insulation boards, damage to composite geomembranes, blockage of drainage pipes, and increasing frost heaving performance of gravel filled with fine soil (Chen et al., 2023; Ming et al., 2023). It should be emphasized that these measures are primarily proposed with the aim of mitigating frost heave in canal foundation soil and can be applied to various cold region engineering. Therefore, it is imperative to incorporate the frost damage characteristics of the canal lining and put forward targeted proactive measures for minimizing frost damages.

The tests showed a strong ice bonding effect at the interface between frozen soil and lining during freezing, leading to complex interactions (Wang et al., 2019). Their interactions are examined by developing frost heave models based on soil frost heave tests and direct shear tests between them (Liu et al., 2020; Pan et al., 2022). The canal lining mainly bears the frost heave forces and freezing forces generated by frozen soil.

The lining can be simplified as a simply supported beam, the freezing force can be determined by considering factors such as soil temperature, water content, and lining material properties. Then, an analytical model is developed to assess frost dagame to the canal lining (Wang, 2004; Jiang et al., 2022b). To accurate analyze the interaction between lining and frozen soil, a frost heave analytical model for the canal lining is established based on elastic foundation beam model (Jiang et al., 2022a). To further investigate the dynamic interaction between lining and frozen soil, a nonlinear contact model for lining-frozen soil is proposed. Then, based on the principles of heat-water-mechanical coupling in frozen soil, a numerical model to simulate canal frost heave is established (Liu et al., 2020; Jiang et al., 2022c; Shi et al., 2023). Through these theoretical models, it has been found that canals with arc-shaped toe, arc bottom, or wide-shallow cross-sections experience lower normal frost heave force compared to narrow-deep trapezoidal canals. Consequently, narrow-deep trapezoidal canals are seldom employed or transformed into arc sections in new canal projects or renovation projects (Chen et al., 2023; Jiang et al., 2022b). In addition, the frost damage of the lining can be mitigated by reducing its structural stiffness, and an anti-frost heave measure of setting longitudinal seams at the position of the lining maximum deformation is proposed (Jiang et al., 2019). This measure has been widely adopted in engineering projects and has been included in the Chinese code. Moreover, the freezing force at the canal lining-frozen soil interface is the main cause for lining frost heave; thus, regulating freezing force becomes crucial to control lining frost heave and reduce its damage. In view of this finding, a preliminary proposal has been made for a two-layer composite geomembrane lining structure (TLCGLS) aimed at mitigating frost damage (Wang et al., 2019).

TLCGLS consists of a canal lining and two-layer composite geomembranes (TLCGs; Fig. 2a), and it replaces the single-layer composite geomembrane utilized in existing projects with TLCGs. The composite geomembrane can be classified into two forms: one comprising a geotextile and a geomembrane, and another consisting of two geotextiles and a geomembrane. In cold reasons, the upper layer of TLCGs is frozen in conjunction with the lining, while the lower layer of TLCGs is frozen together with the canal foundation soil. By the reduced friction between TLCGs, the freezing constraint between the lining and frozen soil is minimized, thereby mitigating frost heave forces and achieving a reduction in canal damage (Wang et al., 2019). Through theoretical analysis, it can be inferred that TLCGLS can reduce the effect of the uneven frost heave of the canal foundation soil on the lining during freezing (Fig. 2b). In addition, TLCGLS may has good resetting ability for the lining with negligible sliding phenomenon during melting (Fig. 2c). Moreover, TLCGs offer an extended service life, improved anti-seepage
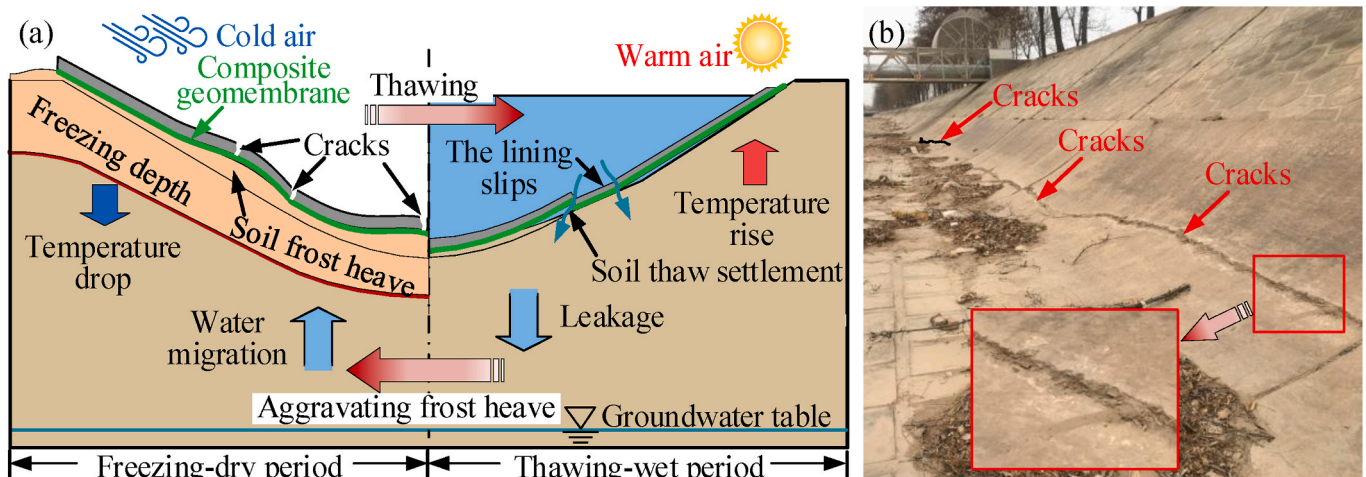

Fig. 1. Frost damage to canals: (a) process of frost damage; (b) paragraph of frost damage.
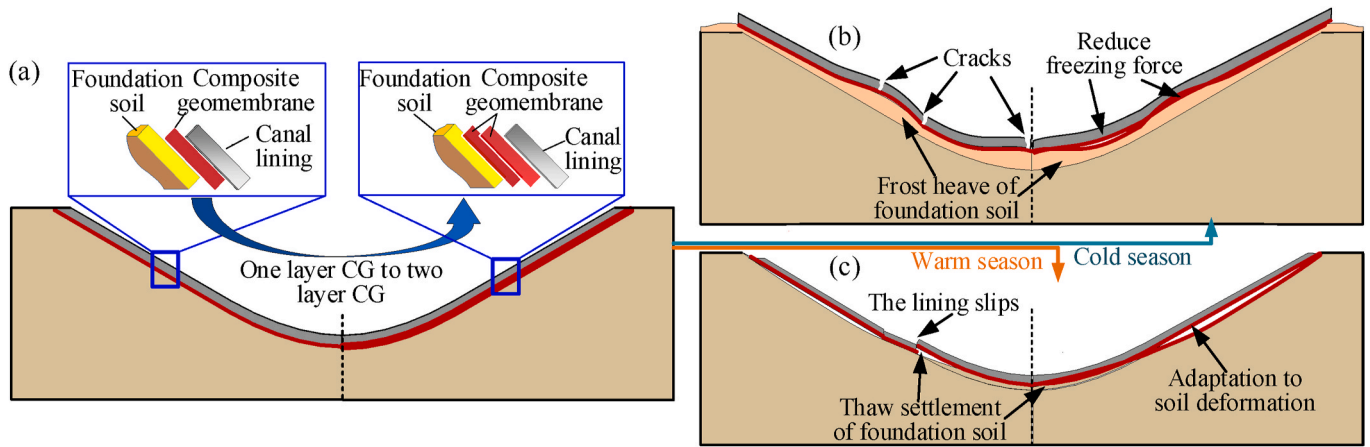
Fig. 2. Anti-frost heave schematic diagram of TLCGLS: (a) structural arrangement; (b) frost heave; (c) thaw settlement.

performance, and enhanced anti-frost heave performance of TLCGLS. Consequently, TLCGLS exhibits significant potential for engineering applications. However, the anti-frost heave performance of TLCGLS has only been subjected to a preliminary theoretical analysis (Wang et al., 2019), lacking experimental verification and an accurate theoretical calculation model, while the anti-frost heave mechanism remains unclear.

In this study, canal frost heave model tests were conducted to validate the efficacy of TLCGLS in reducing frost damage. Then, a nonlinear contact model was proposed for the interaction among canal lining, TLCGs, and canal foundation soil, followed by establishing a frost heave model with heat-water-mechanical coupling for TLCGLS. Finally, the influence of canal cross-section shapes and arrangements of TLCGs on the anti-frost heave performance of TLCGLS as well as its mechanism were discussed.

2. Model test

2.1. Model test configuration

2.1.1. Model test system

The experiments were conducted in a low-temperature environmental simulation system, consisting primarily of two temperature control systems, a model slot, and a data acquisition system (Fig. 3). The

temperature control systems employ compressors for refrigeration to maintain the box at temperatures ranging from -40 to $60\,°C$ with less than $1\,°C$ uniformity. It also allows the cool both to sustain temperatures ranging from -30 to $40\,°C$ with an accuracy level of $\pm 0.1\,°C$.

The interior dimensions of the model slot measure 140 cm in length, 60 cm in width, and 115 cm in height. It is made of stainless steel with asbestos lining on the sides and bottom for insulation. The bottom of the slot has an aluminum plate with a circulation channel connected to a cool both for temperature control. The top of the aluminum plate has a closed-loop water channel connected to a Markov bottle for supplying water to experimental model.

To investigate the heat, water, deformation, and strain responses of the canal under sub-zero temperature conditions, a set of sensors was employed. These included temperature sensors (manufactured by the Key Laboratory of Cryospheric Science and Frozen Soil Engineering in China), volumetric water content sensors (EC-5 sensors, manufactured by METER Inc., USA), displacement sensors (manufactured by Shenzhen Hongmei Technology Inc., China), and strain gauges (manufactured by Chengdu Electric Measurement and Sensing Technology Inc., China). The detailed specifications of these sensors are presented in Table 1. The strain gauge is connected in a half-bridge configuration, incorporating an additional temperature compensation strain gauge to mitigate the impact of temperature fluctuations on its measurements. Prior to the experiment, the sensors were strictly calibrated, and data were collected
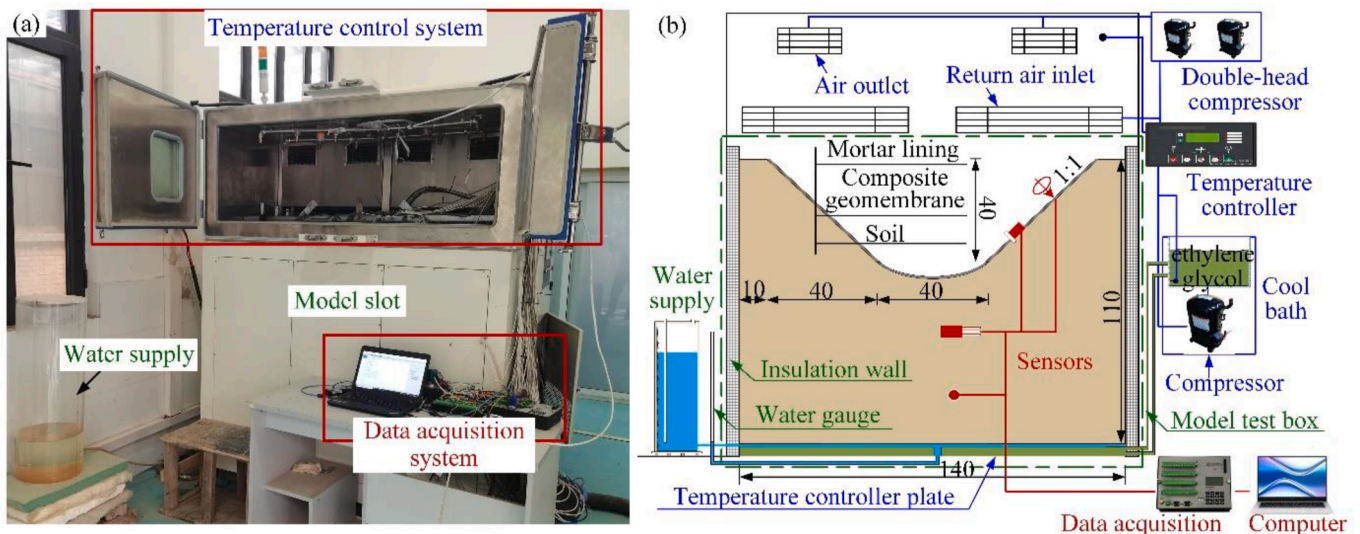

Fig. 3. Experimental system and model design: (a) experimental apparatus; (b) schematic sketch of model test (unit: cm).

Table 1
Detailed specifications of the sensors.

Sensor	Observation content	Range	Precision
Temperature sensor	Temperatures of soil and lining	−30~30 °C	±0.05 °C
Volumetric water content sensor	Volumetric water content of soil	0~1 m³/m³	±0.03 m³/m³
Displacement sensor	Displacements of soil and lining	0~100 mm	±0.05% F.S
Strain gauge	Lining strain	0~20,000 μm/m	±0.1% F.S

using the CR3000 data logger (Campbell Scientific Inc., USA) at a sampling rate of 10 min per interval. These sensors and data logger constituted the data acquisition system for this experiment.

2.1.2. Model materials and design

The anti-frost heave performance of TLCGLS was evaluated using two canal models (Case 1 and Case 2) constructed in the model slot. Each model had dimensions of 140 cm length, 110 cm height, and 30 cm width (Fig. 3b). The composite geomembrane used for testing was a commonly manufactured product in the manufacturing industry, primarily employed for water seepage prevention in hydraulic engineering.
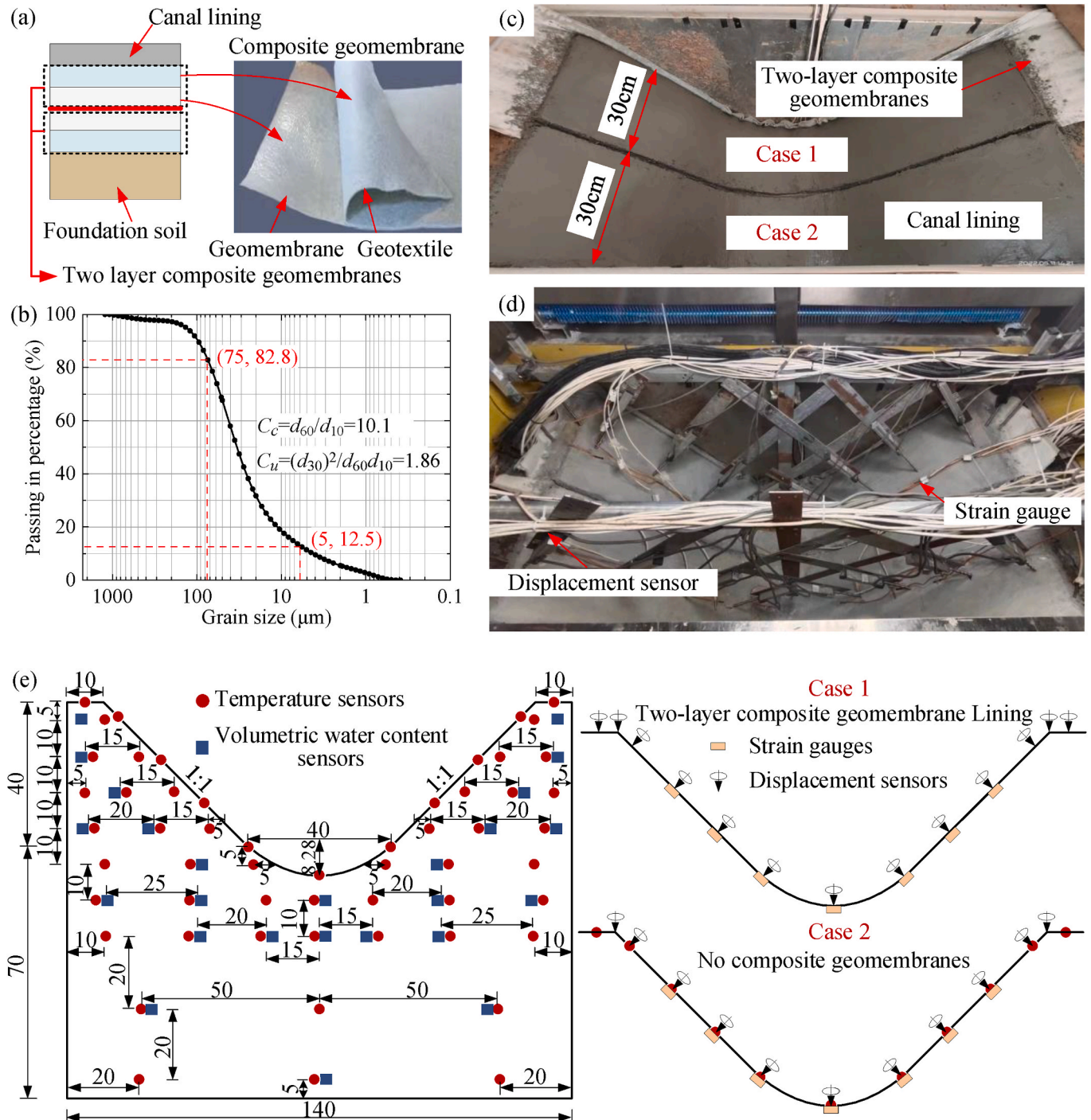

Fig. 4. Physical model test of the canal: (a) configuration of TLCGLS; (b) particle size distribution of the soil; (c) canal model after the lining construction; (d) canal model after the sensors installation; (e) layouts of the sensors (unit: cm).

It comprised of a polyethylene geomembrane and a non-woven geotextile, with a mass per unit area of 400 g. The non-woven geotextile was made of polyester fibers, while the thickness of the geomembrane measured 0.3 mm. This composite geomembrane exhibited a breaking strength of approximately 7.5 kN/m and a breaking elongation of around 60%. In Case 1, TLCGs with geomembrane-geomembrane contact were installed between the canal lining and foundation soil (Figs. 3b and 4a), and the thickness of the geomembranes measured 0.6 mm. Conversely, in Case 2, no composite geomembrane was interposed between them. Based on preliminary tests prior to this experiment, it was determined that the freezing depth of the canal measured approximately 18 cm; this is roughly 1/10 compared to that observed in northwestern China. Consequently, in this experiment, the lining thickness was reduced to 1/10 (equivalent to 1.2 cm) of the actual engineering lining thickness and implemented as an in situ cast lining plate.

The test soil was frost-sensitive silt, and its particle size distribution curve is shown in Fig. 4b. The clay content was 10.4%, while the silt content was 72.4%. In addition, the liquid limit, plastic limit, maximum dry density, and optimum water content were determined as 28.7%, 17.5%, 1.73 g/m³, and 18.2% respectively. The soil sample was thoroughly mixed with water and sealed in a container for 3 days to ensure uniform water distribution throughout the sample. Subsequently, a soil sample with an approximate mass moisture content of 20% was prepared. The canal lining was constructed using a cement mortar mixture of 1 part cement (32.5 ordinary Portland cement), 2 parts sand, and 0.5 parts water.

The canal model was compacted in layer to achieve approximately 85% compaction degree. Each layer underwent compaction with a flat plate rammer to reach a filling height of 10~15 cm. Then, the sensors were buried in designated locations, and shaving treatment was performed between each layer. When the filling height reaches 110 cm, the soil canal was constructed according to specified dimensions. In Case 1, TLCGs were placed on the surface of canal foundation soil, followed by the application of mortar. In Case 2, mortar was directly applied to the canal surface. The lining joints were meticulously cut to prevent interaction between Cases 1 and 2 (Fig. 4c). After a 7-day maintenance period, strain gauges were attached to the lining, and a displacement sensor shelf was built for securing displacement sensors (Fig. 4d). The Markov bottle's height matched that of the model bottom, and then the model remained at a temperature of 10 °C for 7 days to ensure stability in terms of temperature, water content, and deformation. Considering minimal impact from TLCGs on temperature and water distribution during winter within the waterless canal, only temperature and water sensors were positioned within the canal foundation soil under Case 2. The sensor arrangement is shown in Fig. 4e.

2.1.3. Schemes of model test
Considering the temperature conditions in northwestern China,

freezing and melting temperatures were chosen as −15 °C and 10 °C respectively, with the aluminum plate at the bottom of the canal maintained at 10 °C (Jiang et al., 2022c; Zhang et al., 2021). Combined with the temperature design in previous studies (Zhang et al., 2021), the designed and monitored ambient temperatures are shown in Fig. 5a. The designed ambient temperature can induce a certain freezing depth and frost heave in the canal, which then complete melts during melting. Currently, meeting the similarity criterion for heat-water-deformation coupling of frozen soil and its interaction with structures is challenging. Therefore, this study primarily focuses on elucidating the effectiveness of TLCGLS through mechanistic explanations without strictly adhering to the similarity criterion.

To demonstrate the reproducibility of temperature control in this experimental setup, multiple tests were conducted on both the box and cool bath temperatures as depicted in Fig. 5b. The positions of the air outlet and inlet in the box were fixed to ensure a consistent flow field, enabling accuracy testing at any location within the box. In terms of the cool bath, the internal refrigerant maintained a constant temperature, ensuring that variations in testing position did not affect temperature results. As shown in Fig. 5b, the temperature settings of the experimental setup aligned with the requirements of this experiment, and the temperature data was collected using a CR3000 data logger. The testing temperature of the box aligns closely with that of this experiment, showing a data range below 0.8 °C with an accuracy within ±0.4 °C. Similarly, the test temperature of the cool bath aligns closely with the set temperature, exhibiting a temperature range below 0.2 °C and an accuracy within ±0.1 °C. Therefore, this experimental setup ensures repeatability in temperature control.

2.2. Model test results

The phenomenon of frost heave in canal foundation soil is a dynamic process that involves the complex interaction of water, heat, and deformation. It primarily encompasses temperature reduction, water migration, ice-water phase transition, and subsequent deformation (Jiang et al., 2022c; Li et al., 2022). Therefore, an analysis of temperature variations, water content, and deformation is conducted to evaluate the anti-frost heave effectiveness of TLCGLS.

2.2.1. Analysis of the temperatures
The temperature, water, and deformation fields of the canal in this experiment exhibits symmetry along its central axis at the bottom. Therefore, Fig. 6 only presents the temperature distribution on the left half of the canal based on temperature sensor measurements at key time points.

As shown in Fig. 6a, the temperature at 0h is about 10 °C, meeting the initial temperature requirements. At 186h (Fig. 6b), a frozen zone forms with freezing depths of 24 cm at slope A, 14 cm at slope toe B, and
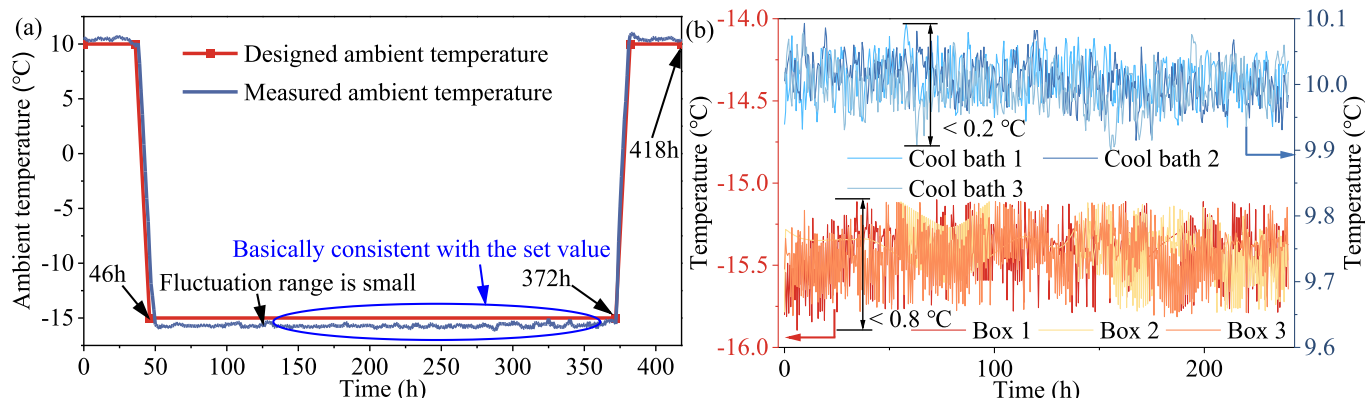

Fig. 5. Temperature variations with time: (a) designed and measured ambient temperature; (b) existing temperature measurements of box and cool bath.
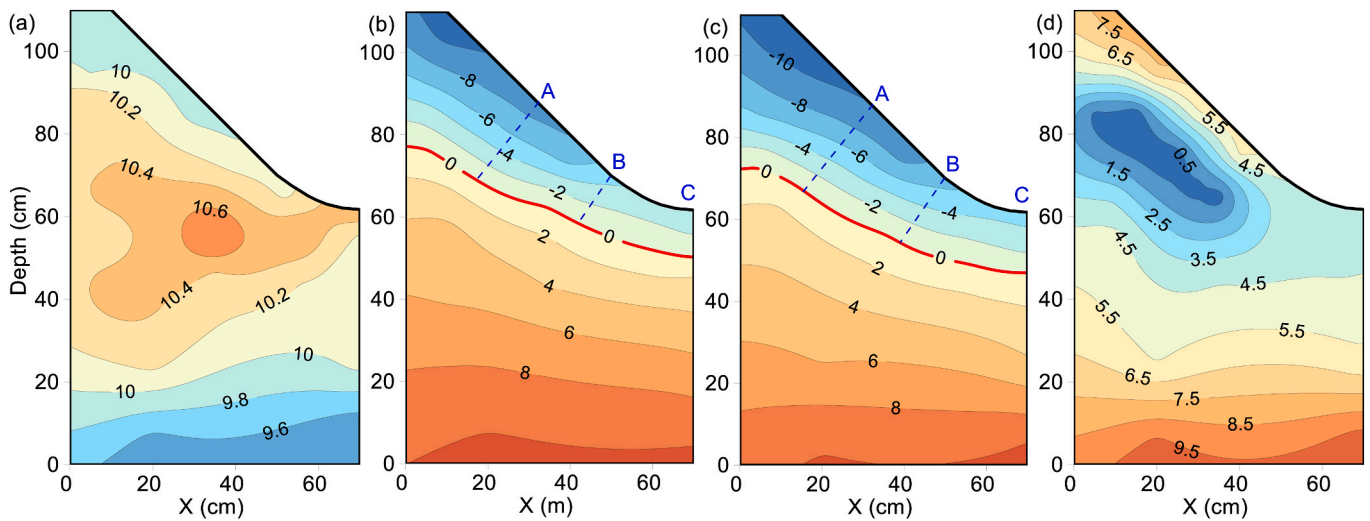
Fig. 6. Temperature distributions at critical moments: (a) 0 h; (b) 186 h; (c) 372 h; (d) 418 h.

11 cm at bottom C. At freeze completion (372h, Fig. 6c), the freezing depths at slope A, slope toe B, and bottom C were measured to be 28 cm, 19 cm, and 15 cm respectively. Notably, freezing depth on slopes exceeds that at the bottom of the canal. After 46 h of continuous melting (418h, Fig. 6d), the canal temperature rises above 0 °C, leading to the elimination of the frozen zone and a significantly accelerated rate of thawing compared to freezing. The temperature contour line is basically parallel to the canal slope. Except for rapid temperature fluctuations in frozen regions, minimal variations are observed in other areas, while maintaining a relatively constant temperature at the canal bottom. Overall, the temperature distribution and freezing depth development are basically consistent with field measurements (Chen et al., 2023; Jiang et al., 2022c), indicating that the temperature control and results of this experiment align with engineering practice.

The temperature variations over time are further analyzed by selecting key points at the bottom, slope, and top of the canal, as depicted in Fig. 7. The air temperature near the canal surface exhibits rapid changes in response to variations in ambient temperature, closely aligning with the ambient temperature, indicating excellent temperature uniformity in the model slot. As soil depth increases, there is a gradual decrease in the temperature change rate. During the freezing-melting process, canals undergo temperature fluctuations, including rapid decline, gradual decrease, and subsequent elevation. During the freezing period, the temperature on the surface of the canal top is lower than that of the slope surface, which in turn is lower than that of the bottom surface. The soil freezing rate at the canal top exceeds that on the

slope, which in turn exceeds that at the bottom. During the melting process, the soil melting rate at the canal top surpasses that on the slope, which in turn exceeds that at the bottom. In addition, a horizontal section exists in frozen soil temperature due to heat absorption from phase change between ice and water in the soil. In general, the structural configuration of the canal leads to spatial variations in temperature dynamics, resulting in heterogeneous rates of freezing and melting.

2.2.2. Analysis of the water contents

Fig. 8 presents the unfrozen volumetric water content distribution on the left side of the canal, based on measurements from volumetric water content sensors at 0h, 186h, 372h, and 418h. The model is saturated at the bottom due to groundwater. At 0h (Fig. 8a), the water content increases from top to bottom, similar to the water state before freezing in practice. At 186h (Fig. 8b), the water freezes into ice, leading to a decrease in unfrozen water content in frozen zone. At a distance equivalent to that of the canal surface, the bottom has higher unfrozen water content compared to the slope. Near the slope, the water content is mostly residual. Negative temperature suction near the freezing front induces water migration, leading to a decrease in water content in unfrozen zone. The water content near the freezing front uniformly decreases but does not abruptly drop to a residual value. As the freezing front progresses downward (Fig. 8c), minimal changes in unfrozen water content occur in the frozen zone, while significant alterations are observed near the freezing front. As temperature increases (Fig. 8d), melting is observed in locations other than near the slope. Comparing
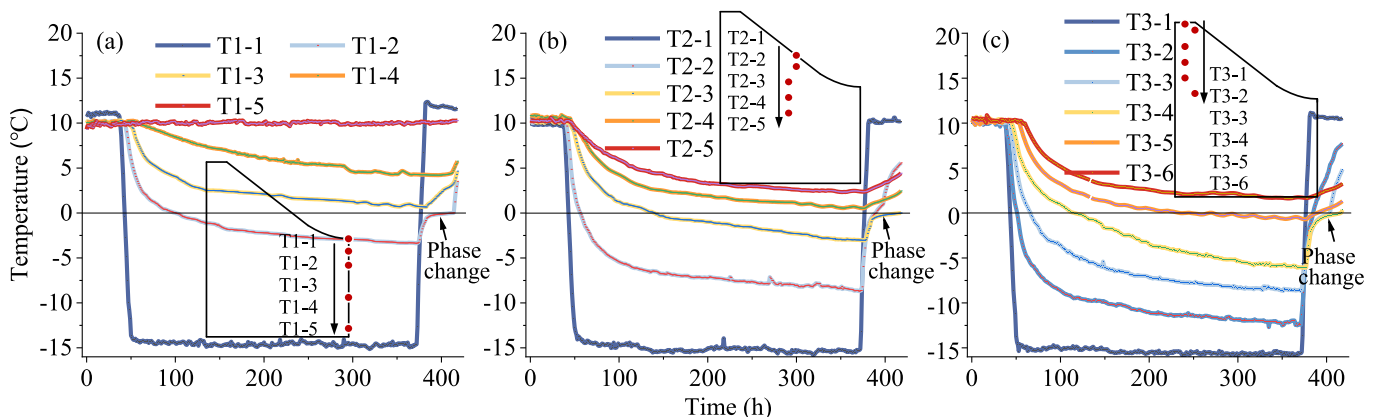

Fig. 7. Temperature variations with time at critical positions: (a) canal bottom; (b) canal slope; (c) canal top.
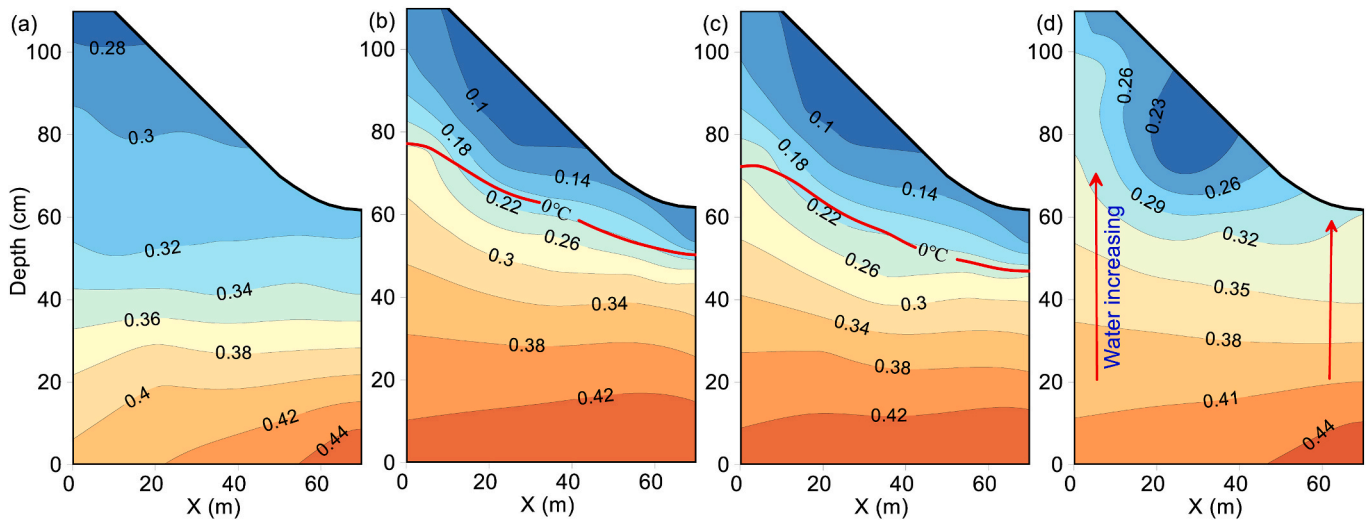
Fig. 8. Unfrozen volumetric water content distributions at critical moments: (a) 0h; (b) 186h; (c) 372h; (d) 418h.

the water content distribution at 0h (Fig. 8a), a significant increase can be seen within the arrow region (Fig. 8d), which can be attributed to the water migration. Water migration at the bottom exceeds that at the top due to its slower freezing rate. Overall, there are significant variations in water content within and around the frozen zone, while minimal changes occur in other zones.

To further investigate the evolution of water content in the canal foundation soil during the freezing-thawing process, the water content variations over time of representative locations are shown in Fig. 9. At the onset of freezing (36h), the water content remains relatively stable, meeting the pre-test requirements. As ambient temperature decreases, the surface water content declined rapidly, while the water response decelerates with increasing soil depth. It is noteworthy that soil freezing also leads to a decrease in water content within adjacent unfrozen zone, which indicates a significant water migration from the unfrozen to frozen zones. During the melting process, the water content in the frozen zone increases rapidly, and the resulting water leakage also leads to an elevation in water content in the unfrozen zone. Following melting, the water content in the previously frozen zone increases, especially near the freezing front. Generally, the canal experiences a process of rapid decline, gradual decline (or basic stability), and subsequent rapid increase in water content. The variations in water migration caused by the freezing rate of the canal lead to significant water redistribution phenomena.

2.2.3. Analysis of the deformations and strains

The deformation behavior of the canal lining can effectively demonstrate the anti-frost heave performance of TLCGLS. Fig. 10a presents the distributions of normal frost heave along the cross-section of the lining at critical moments under two Cases. As shown in Fig. 10a, during the freezing process at 84h and 168h, there exists a slight deformation difference between the two Cases. However, Case 1 (TLCGLS) exhibits greater deformation compared to Case 2 (no composite geomembrane: NCG). At the maximum freezing depth (372h), significant deformation difference between the two Cases emerges, particularly at the canal bottom where it reaches up to 15%. Case 1 experiences higher frost heave at the canal bottom than Case 2, while Case 1 shows lower frost heave on the slope compared to Case 2. To quantify uneven frost heave within the lining, the mean square error is introduced, as shown in Eq. (1). The mean square error of deformation for the slope under Case 1 and Case 2 is calculated as 0.11 and 0.17 respectively, exhibiting a reduction rate exceeding 35%; the canal bottom exhibits negligible variation, thereby indicating that TLCGLS can effectively mitigate uneven frost heave in the canal lining. At the final melting moment (418h), the deformation under Case 1 decreases rapidly, with residual deformation smaller than that observed under Case 2, indicating a robust resetting ability of TLCGLS.

$$S[D(\pmb{x})] = \sqrt{E\{D(\pmb{x}) - E[D(\pmb{x})]\}^2} \qquad (1)$$
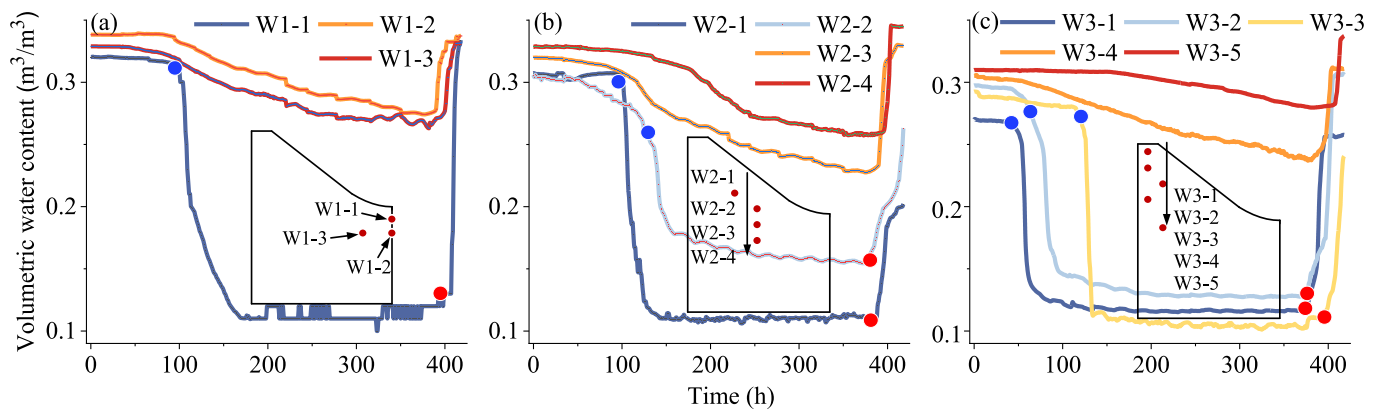

Fig. 9. Unfrozen volumetric water content variations with time at critical positions: (a) canal bottom; (b) canal slope; (c) canal top. The blue dot signifies the onset of freezing, while the red dot indicates the initiation of melting. (For interpretation of the references to colour in this figure legend, the reader is referred to the Web version of this article.)
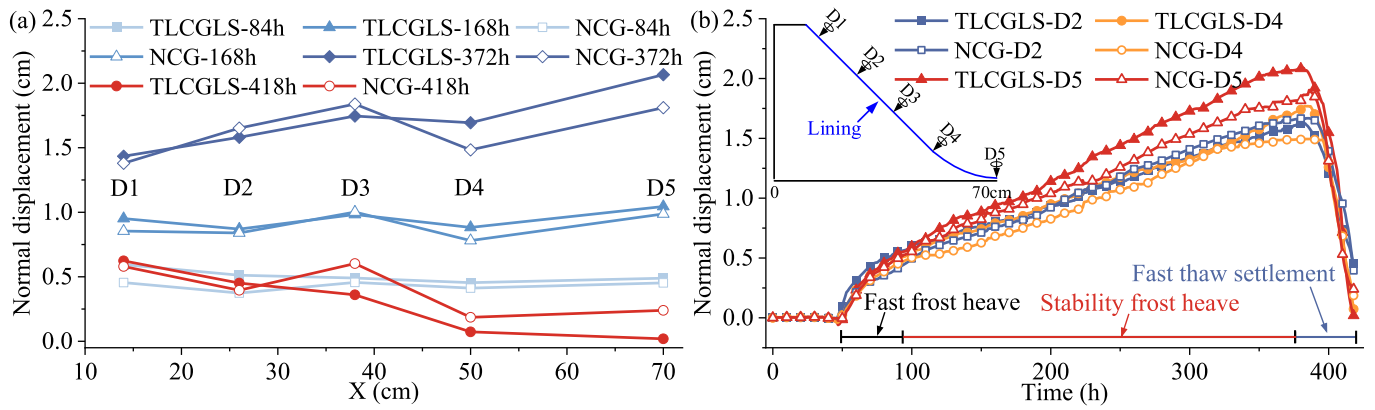
Fig. 10. Normal displacement of the canal lining under Case 1 (TLCGLS) and Case 2 (NCG): (a) lining deformation along its section; (b) deformation variations with time.

where $D(x)$ is the normal deformation; S and E are the mean square error and mean value of the deformation.

The deformation variations of the canal lining at key positions are showed in Fig. 10b. The lining exhibits freeze shrinkage prior to frost heave, and the freezing-thawing process can be categorized into stages of rapid frost heave, stable frost heave, and rapid melting. During the initial stage of frost heave, the deformation of the slope under Case 1 exceeds that observed under Case 2; in the later stage of frost heave, this trend is reversed. In addition, the frost heave at the bottom center under Case 1 consistently exceeds that observed under Case 2. Moreover, an increase in canal frost heave leads to a greater difference in frost heave between the two Cases. During the melting stage, the initiation of lining melting in Case 1 occurs earlier compared to Case 2, accompanied by a higher melting rate and reduced residual deformation. These findings further indicates that TLCGLS has a strong resetting ability during melting.

The relative tangential displacement between the canal lining and foundation soil plays a crucial role in preventing frost heave. This displacement can be determined by calculating the difference between the deformation of the top of the lining and that of the foundation soil, as shown in Fig. 11. During the rapid frost heave stage, there is negligible relative tangential displacement in both Cases. As freezing time increases, Case 1 exhibits an initiation of relative tangential displacement, which undergoes a phase of rapid growth followed by a slower growth stage. Conversely, for Case 2, the relative tangential displacement is significantly smaller compared to Case 1 and demonstrates a gradual increase over time. During the melting stage, Case 1 experiences a rapid reduction in relative tangential displacement; this reduction rate is considerably higher than that observed in Case 2, resulting in a smaller final residual relative tangential deformation for Case 1. Overall, the TLCGLS demonstrates an increased relative tangential deformation

between the lining and foundation soil during freezing stages, which can be promptly restored during the subsequent melting stage.

To further investigate the stress conditions of the canal lining under two Cases, Fig. 12 shows the lining strain distributions at critical moments. The pressure is observed at 48h, and the strain across different positions exhibits a nearly uniform distribution with minimal variation between the two Cases. As freezing time progresses (168h), the compressive strain at the slope toe increases rapidly, while minor changes occur along the slope. Notably, Case 1 exhibits lower compressive strain compared to Case 2. At the moment of maximum freezing depth (372h), the compressive strain at the center of the canal bottom exhibits a rapid increase, while tensile strain is observed at the slope toe and lower part of the slope. Furthermore, it can be noted that the canal lining has reached its peak tensile and compressive strains during this period. Additionally, it should be highlighted that Case 1 exhibits approximately 29% lower maximum compressive strain and 28% lower maximum tensile strain compared to Case 2. At the final melting moment (418h), a rapid decrease in strain is observed, accompanied by residual strain where Case 1 displays smaller values than Case 2. Overall, TLCGLS effectively mitigates lining stress induced by soil frost heave and reduces residual strain after melting, highlighting its remarkable anti-frost heave effect.

3. Numerical simulation

To further investigate the effect of canal cross-section shapes and arrangements of TLCGs on preventing canal frost heave and its anti-frost heave mechanism, a heat-water-mechanical coupling model that incorporates soil frost heave and interaction among the canal lining, TLCGs, and foundation soil.

3.1. Mathematical model

3.1.1. Coupled heat-water transport model

Water migration plays a significant role in causing frost damage to engineering situated on fine-grained soil foundations with high water content (Teng et al., 2023). Conversely, the contribution from vapor transport is approximately two orders of magnitude smaller than total moisture migration (Li et al., 2010). Therefore, for canals constructed on fine-grained soil foundations with high soil water content, the impact of vapor transport on canal frost heave calculations can be ignored. Considering the phase change of ice-water in soil, Fourier's heat transfer equation and Richard's equation could be employed to describe the thermal and hydraulic processes of freezing soil. The equations are as follows (Chen et a., 2022; Harlan, 1973):

$$C_v \frac{\partial T}{\partial t} = \nabla \cdot (\lambda \nabla T) + L_f \rho_i \frac{\partial \theta_i}{\partial t} \tag{2}$$
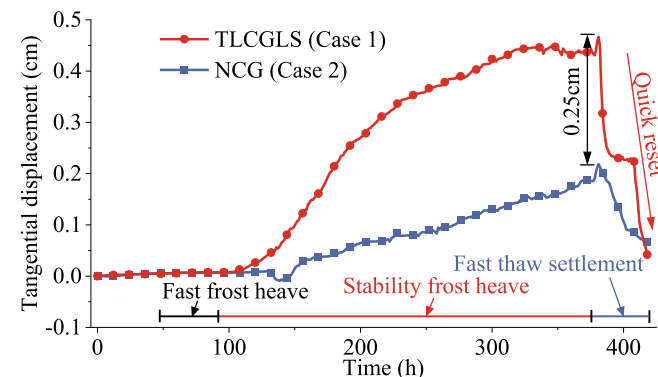

Fig. 11. Tangential displacement of the canal lining under Case 1 and Case 2.
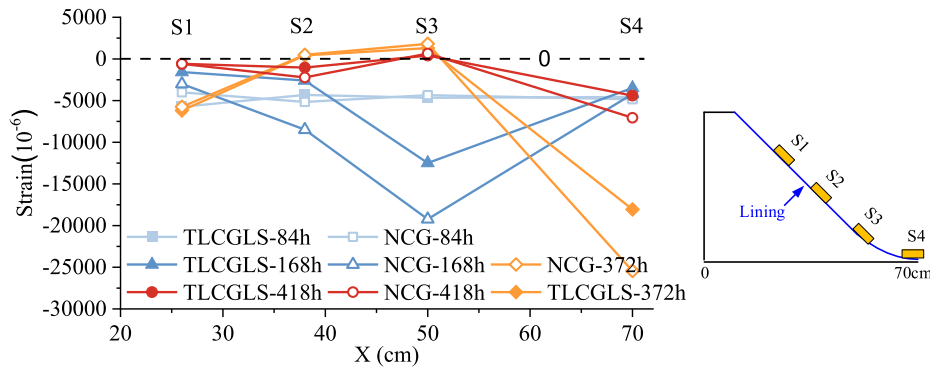
Fig. 12. Stain of the canal lining under Case 1 (TLCGLS) and Case 2 (NCG).

$$C\frac{\partial h}{\partial t} = \nabla \cdot (k\nabla(h + \mathbf{i})) - \frac{\rho_i}{\rho_w}\frac{\partial \theta_i}{\partial t} \tag{3}$$

where T, h, and θ_i are the variables to be solved, representing the temperature, matric potential, and volumetric ice content respectively; ρ_w, ρ_i, L_f, and $\mathbf{i}$ are the water density, ice density, specific latent heat of ice-water phase change, and unit vector in the direction of gravity, respectively; C_v and λ denote the specific heat capacity and thermal conductivity respectively, which can be calculated using Eq. (4)~(5); C and k are the specific moisture capacity and hydraulic conductivity respectively, which can be determined using the van Genuchten model and ice impedance factor (I), as described by Eq. (6)~(8).

$$C_v = \frac{1}{\rho}(\rho_s C_s \theta_s + \rho_w C_w \theta_w + \rho_i C_i \theta_i) \tag{4}$$

$$\lambda = \lambda_s \theta_s + \lambda_w \theta_w + \lambda_i \theta_i + \lambda_a \theta_a \tag{5}$$

$$C = \frac{\alpha m}{1-m} \cdot (\theta_s - \theta_r) \cdot Se^{1/m} \cdot (1 - Se^{1/m})^m \tag{6}$$

$$k = k_s \cdot \sqrt{Se} \cdot \left[1 - (1 - Se^{1/m})^m\right]^2 \cdot 10^{-10\theta_i} \tag{7}$$

$$Se = \frac{\theta_w - \theta_r}{\theta_s - \theta_r} = \left(1 + |\alpha h|^{1/(1-m)}\right)^m \tag{8}$$

where the subscripts a, i, w, and s are different components including air, ice, water, and soil particles respectively; α and m are the empirical parameters; k_s and Se represent the hydraulic conductivity of saturated soil and effective saturation, respectively; θ_s and θ_r denote the volumetric water content at saturation and residual state, respectively.

The soil freezing characteristic curve (Eq. (9)) is used for computing the ice formation rate (Eq. (10)), serving as a correlation equation between Eqs. (2) and (3).

$$\theta_w = \frac{\rho_d}{\rho_w} a|T|^b \tag{9}$$

$$\frac{\partial \theta_i}{\partial t} = -\frac{\rho_w}{\rho_i}\frac{d\theta_w}{dt} = -\frac{\rho_w}{\rho_i}\frac{d\theta_w}{dT}\frac{dT}{dt} \quad T < T_f \tag{10}$$

where ρ_d is the dry density of soil; a and b represent the test parameters, which be obtained by freezing characteristic curve test; T_f is the freezing temperature of soil.

3.1.2. Heat-water-related mechanics model

The stress-strain relationship of freezing soil can be expressed in an incremental function as follows (Arzanfudi et al., 2020):

$$\{\Delta\sigma\} = [D](\{\Delta\varepsilon\} - \{\Delta\varepsilon^p\} - \{\Delta\varepsilon^v\}) \tag{11}$$

where $[D]$ is the elasticity matrix; $\{\Delta\sigma\}$ is the stress increment vector;

$\{\Delta\varepsilon\}$ and $\{\Delta\varepsilon^v\}$ are the strain increment vector and frost heave strain increment vector, respectively; $\{\Delta\varepsilon^p\}$ is the plastic strain increment vector, which can be calculated as follows:

$$\{\Delta\varepsilon^p\} = \lambda_{pu}\frac{\partial Q}{\partial\{\sigma\}} \tag{12}$$

where λ_{pu} is the plastic multiplier; Q is the plastic potential function, which is equivalent to the yield function F of Drucker-Prager yield criterion matched to Mohr-Coulomb criterion.

$$F = \sqrt{J_2} + \alpha_1 I_1 - k_1 \tag{13}$$

$$\alpha_1 = \frac{2\sin\varphi}{\sqrt{3}(3 - \sin\varphi)} \tag{14}$$

$$k_1 = \frac{2\sqrt{3}c\cos\varphi}{(3 - \sin\varphi)} \tag{15}$$

where J_2 and I_1 are the second deviatoric stress invariant and first stress invariant, respectively; c and φ are cohesive strength, internal friction angle, respectively.

During the freezing process, soil exhibits transverse isotropy characteristics, with deformation primarily occurring along the direction of temperature gradient. Consequently, a modification is made to the frost heave strain vector $\{\varepsilon^v\}$ as follows (Liu et al., 2020):

$$\{\varepsilon^v\} = \begin{Bmatrix} \varepsilon^v_{xx} \\ \varepsilon^v_{yy} \\ \varepsilon^v_{xy} \end{Bmatrix} = (\theta_w + \theta_i - n_0)\begin{bmatrix} m_1^2\dfrac{1-\xi}{2} + n_1^2\xi \\ n_1^2\dfrac{1-\xi}{2} + m_1^2\xi \\ m_1 n_1(1 - 3\xi) \end{bmatrix} \tag{16}$$

where n_0 denotes the initial porosity of soil; m_1 and n_1 represent the sine and cosine, respectively, of the angle between the direction of the temperature gradient and horizontal plane; ξ is the partition coefficient of soil frost heave.

3.1.3. Frozen soil-TLCGs-canal lining interaction model

In Case 1 (TLCGLS), the upper and lower composite geomembranes are frozen together with the canal lining and foundation soil, respectively. Their interaction occurs between TLCGs. This interface is considered as the contact zone where normal and tangential forces can represent its mechanical behavior. The normal frost heave force can be transmitted across the interface, while the transfer of the normal freezing force is impeded, resulting in a separation when the normal deformation of the lining exceeds that of soil. The tangential freezing force can transmit through the interface friction. If the tangential force exceeds the tangential freezing strength, slippage may occur at the interface. In this study, the elastic thin layer model was modified to accurately describe the interaction between lining and frozen soil with

TLCGs.

The elastic thin layer model is based on normal and tangential spring elements at the contact interface between structures, where the spring stiffness can exhibit nonlinear variation in response to deformation. By calculating the contact reaction between structures based on their relative displacement, further adjustments are made to refine their displacement. Compared to the commonly employed contact interface algorithm, this model simplifies the dynamic interface search process by transforming it into a static elastic problem, particularly by considering dynamic friction as tangential spring stiffness. This approach facilitates program convergence and maintains a certain level of realism. The basic equations are as follows:

$$\sigma_n = - k_{An}(u_{nl} - u_{ns}) \tag{17}$$

$$\sigma_t = - k_{At}(u_{tl} - u_{ts}) \tag{18}$$

where σ_n, σ_t are the normal and tangential spring reactions, respectively; k_{An}, k_{At} are the normal and tangential spring stiffness, respectively; u_{nl}, u_{tl} are the normal and tangential displacements of the lining, respectively; u_{ns}, u_{ts} denote the normal and tangential displacements of the soil, respectively. Based on the mechanical behavior between TLCGs, modifications are made to k_{An} and k_{At} in Eq. (19) ~ (20). The differences in different arrangements of TLCGs primarily manifest in the tangential parameters, while the normal parameters remain consistent.

$$k_{An} = \begin{cases} E_s, u_{nl} - u_{ns} < 0 \\ 0, u_{nl} - u_{ns} \geq 0 \end{cases} \tag{19}$$

$$k_{At} = \begin{cases} k'_{At}, \sigma_t < \tau_f \\ f \cdot \dfrac{\sigma_n}{|u_{tl} - u_{ts}| + \varepsilon'}, \sigma_t \geq \tau_f \end{cases} \tag{20}$$

where E_s is the soil elasticity modulus; τ_f is tangential strength; k'_{At} is the tangential spring stiffness; f is the dynamic friction coefficient; ε' is an infinitesimally small positive number.

3.1.4. Model implement

The heat-water process can be resolved by solving Eqs. (2), (3) and (10). Real-time updates of the heat-water parameters in Eq. (4)~(9) can be based on the volumetric changes of soil components, ultimately obtaining the distributions of temperature, unfrozen water content, and ice content in canal foundation soil. For the mechanical analysis of a canal with TLCGLS, 1) the mentioned variables are used as inputs for Eq. (16) to calculate frozen strain vector; 2) based on Eq. (11)~ (12), the frost heave of canal foundation soil can be determined; 3) by solving Eq. (17)~(20), the deformation from canal foundation soil can be transferred to the lining, ultimately yielding stress and deformation of the canal lining. Due to the low self-weight of the canal lining, the influence of stress on temperature and water content was not considered. The model exhibits strong nonlinearity and can be numerically solved by COMSOL Multiphysics software. The governing equations can be obtained by the following:

$$d_a \frac{\partial \xi}{\partial t} + \nabla \cdot \mathbf{\Gamma} = S \tag{21}$$

where ξ is the solved variable (T, h, σ); d_a and S are the damping coefficient and source term; $\mathbf{\Gamma}$ is the conservative flux. The generalized solution is as follows:

$$\left(d_a \frac{\partial \xi}{\partial t}, \overline{\xi} \right)_\Omega + (\nabla \cdot \mathbf{\Gamma}, \overline{\xi})_\Omega = (S, \overline{\xi})_\Omega \tag{22}$$

where $\overline{\xi}$ and Ω are the virtual primary variable and computed domain.

The backward Euler difference method is utilized to achieve temporal discretization, and Eq. (17) can be determined by the following:

$$\left(d_a \frac{\xi^i - \xi^{i-1}}{\Delta t}, \overline{\xi} \right)_\Omega - (\mathbf{\Gamma}, \nabla \overline{\xi})_\Omega = (S, \overline{\xi})_\Omega + (\mathbf{n} \cdot \mathbf{\Gamma}, \overline{\xi})_{\partial\Omega} \tag{23}$$

where $\mathbf{n}$, i, $\partial\Omega$ are the outward normal vector of the boundary, time, and boundary domain, respectively.

The initial condition and boundary conditions (Dirichlet and Neumann) are as follows:

$$\xi(x, y, 0) = \xi_0 \tag{24}$$

$$\mathbf{n} \cdot \mathbf{\Gamma} = H_1 + \left(\partial \mathbf{\Pi} / \partial \xi \right)_\mu^T \tag{25}$$

where H_1 and μ are the source term at boundary and Lagrange multiple; the last term is the elastic constraint.

In numerical simulations, the General Form PDE interface in the Mathematics module of COMSOL Multiphysics is used to solve the above PDEs. The Solid Mechanics interface in the Structural Mechanics module was used to analyze soil deformation and its interaction with the canal lining.

3.2. Model validation

3.2.1. Contact model between TLCGs

The direct shear test results between geotextiles under a normal stress of 20 kPa (Li et al., 2003) were used to validate the rationality of the proposed contact model. The estimated parameters for Eq. (20) based on the test results are as follows: $\tau_f = 0.01$ MPa, $k'_{At} = 10$ MPa/m, shear relative displacement when dynamic friction occurs is 2 mm, and $f = 0.43$. Fig. 13a shows the size, mesh, and boundary conditions of the finite element (FE) model, while Fig. 13b shows the numerical results. As shown in Fig. 13b, the ultimate shear strength is 0.01 MPa at a corresponding relative shear displacement of 1 mm. Upon reaching a relative shear displacement of 2 mm, dynamic friction sliding occurs and the friction force stabilizes at a constant value. Notably, the numerical results align closely with the test outcomes.

The direct shear test results between geotextile and geomembrane under normal stresses of 50 kPa and 100 kPa (Muluti et al., 2023) were further used to validate this contact model. The estimated parameters in Eq. (20) under 50 kPa are as follows: $\tau_f = 0.04$ MPa, $k'_{At} = 4.41$ MPa/m, shear relative displacement when dynamic friction occurs is 18 mm, and $f = 0.52$. Similarly, the estimated parameters in Eq. (20) under 100 kPa are as follows: $\tau_f = 0.07$ MPa, $k'_{At} = 6.12$ MPa/m, shear relative displacement when dynamic friction occurs is 20 mm, and $f = 0.44$. The FE model is depicted in Fig. 13a, and the comparison results between numerical simulations and tests are presented in Fig. 13c. As shown in Fig. 13c, the computed stress-displacement relationships agree well with the test results, and the results exhibit only a slight difference in value. Moreover, these relationships align closely with previous research on geomembrane-geotextile interactions (Shi et al., 2020; Xu et al., 2023), providing additional evidence supporting the applicability of this model in accurately predicting contact behavior between TLCGs.

3.2.2. Frost heave model of a canal

Based on the canal frost heave test presented in *Section 2*, a FE model is established as depicted in Fig. 14. The minimum grid size along the temperature gradient direction within the freezing depth range is set to
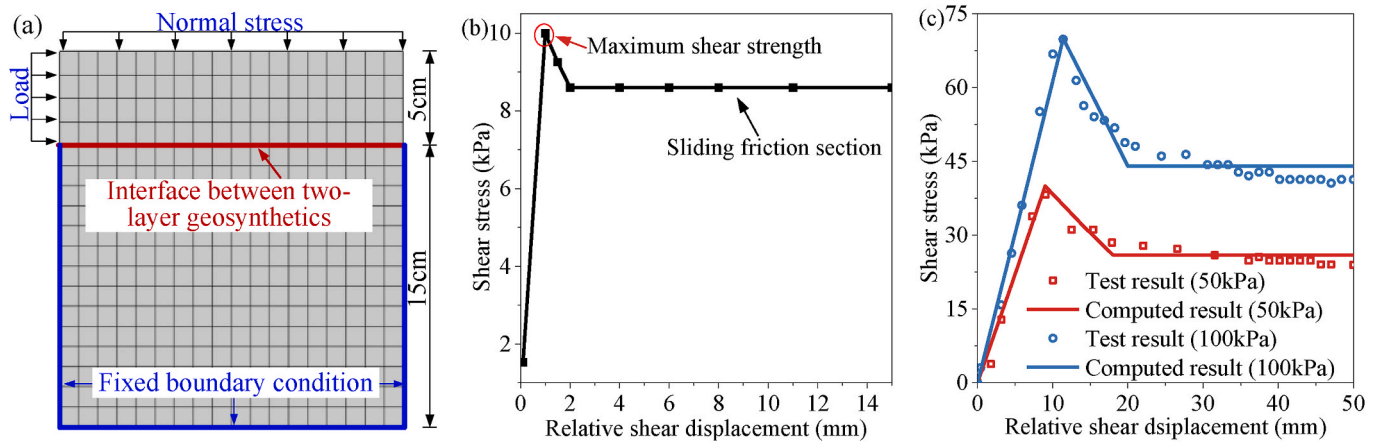
Fig. 13. Validation of the contact model : (a) FE model; (b) computed results between geotextiles; (c) comparison results between geotextile and geomembrane.
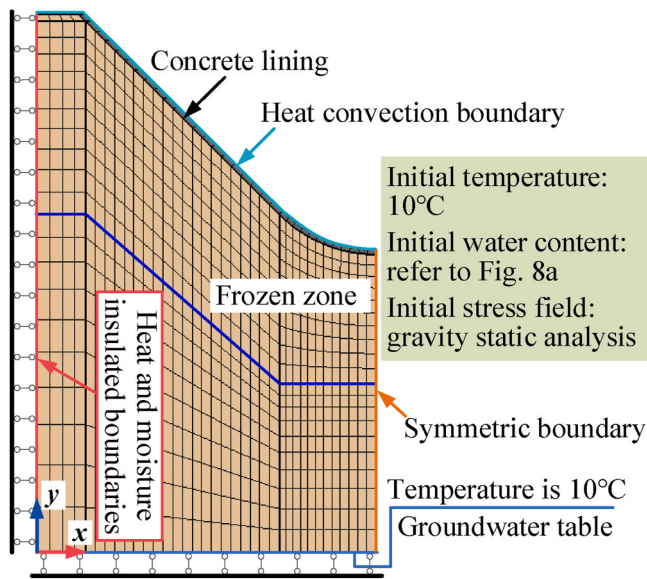

Fig. 14. Meshing, initial and boundary conditions of the FE model. The grid density in the frozen zone has been adjusted to a lower level for the purpose of observation.

Table 2
Soil index properties of test samples.

Variables	Value	Variables	Value
ρ_s (kg/m³)	2700	L_f (kJ/kg)	334
ρ_w (kg/m³)	1000	θ_s (1)	0.43
ρ_i (kg/m³)	931	θ_r (1)	0.10
C_s (kJ/(m³ • K))	2484	α (1/m)	0.38
C_w (kJ/(m³ • K))	4200	m (1)	0.36
C_i (kJ/(m³ • K))	1955.1	k_s (m/s)	1×10^{-7}
λ_s (W/(m • K))	1.5	a (1)	6.8988
λ_w (W/(m • K))	0.6	b (1)	−0.4735
λ_i (W/(m • K))	2.2	c (kPa)	10.0
λ_a (W/(m K))	0.024	φ (°)	20

be 0.5 cm. Fig. 14 shows the initial and boundary conditions for the temperature, water, and stress fields of the canal, with a maximum time step of 100s.

According to the results of soil-water characteristic curve test, freezing curve test, and triaxial compression test, the soil parameters presented in Table 2 were determined (Liu et al., 2020). The soil dry density is 1600 kg/m³. The relationships between the elastic modulus

(E_s) and Poisson's ratio (ν_s) with temperature were calculated as follows (Bai et al., 2020):

$$E_s = \begin{cases} 20 + 11.3(T_f - T)^{0.6} & T \le T_f \\ 20 & T > T_f \end{cases} \tag{26}$$

$$\nu_s = \begin{cases} 0.33 - 0.007(T_f - T) & T \le T_f \\ 0.33 & T > T_f \end{cases} \tag{27}$$

For mortar lining, its elastic modulus and Poisson's ratio are 0.92 GPa and 0.2 respectively, with a density of 2300 kg/m³, thermal conductivity of 1.58 W/(m·K), and volumetric heat capacity of 2231 kJ/ (m³·K).

The Neumann boundary condition is used to calculate the boundary heat flux on the canal surface. The ambient temperature is determined by Fig. 5b. The convective heat transfer coefficient, assumed as 15 W/ m²•K at the top of the canal and 10 W/m²•K at its bottom; a quadratic function is employed to smoothly transition the convective heat transfer coefficient at intermediate positions between the top and bottom.

Fig. 15 shows the comparison results of the temperature, water content, and deformation between the numerical simulation and model test at 186h and 372h. The computed temperature closely matches the monitoring results with minimal deviation. This discrepancy may arise from variances in the selection of convective heat transfer coefficient at the upper boundary of the canal compared to its experimental value, as well as temperature fluctuations at the bottom during test. Nevertheless, both datasets demonstrate consistent patterns. Disparities arise in water content at W1-2 at 168h, while significant differences occur in deformation at the top of the canal slope at this time. These variations could be attributed to the mean moisture content of soil within a 5 cm radius as determined by the water sensor and initial elevated water content resulting from local geological conditions during test. However, for other locations, computed results exhibit minor discrepancies compared to monitoring results for both water content and deformation; their overall trends align well with monitoring results. Therefore, the proposed heat-water-mechanical coupling model can accurately predict frost heave behaviors of canals with TLCGLS.

4. Discussion on the applicability of TLCGLS

4.1. Engineering background and model configuration

To further investigate the applicability of TLCGLS in engineering, a large-scale water conveyance canal located in Ningxia Hui Autonomous Region, China has been selected as the engineering background. The proposed numerical model is used to discuss the suitability of TLCGLS for different canal cross-section shapes and assess the effect of various arrangements of TLCGs on mitigating canal frost heave. The designed
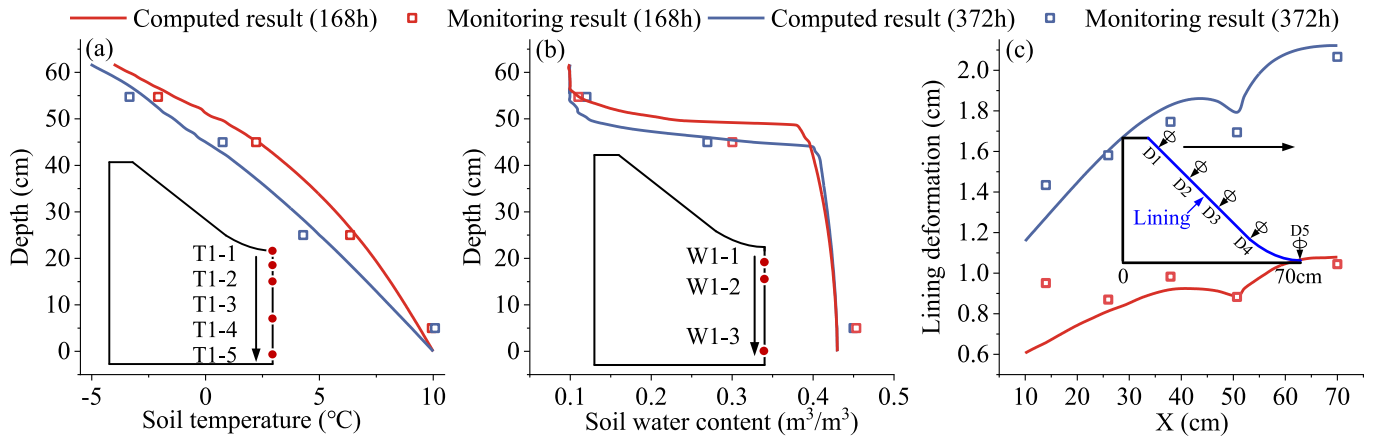
Fig. 15. Comparisons between the computed results and monitoring results: (a) soil temperature; (b) soil water content; (c) lining deformation.

discharge (Q) of the canal is 70 m³/s, with a slope coefficient (m_2) of 1.5, roughness coefficient (n_2) of 0.015, hydraulic slope (i_2) of 1/1500, and freeboard (Δh) of 0.5 m. The lining consists of C30 concrete with a thickness of 12 cm, while the groundwater table remains 2 m below the canal bottom. To ensure comparability of different shape canals, the optimal hydraulic section equations commonly employed in design periods were used to determine the dimensions of trapezoidal canal (Eq. (28)) and arc-bottomed trapezoidal canal (Eq. (29)). Their FE models are depicted in Fig. 16.

$$\beta = 2\left(\sqrt{1 + m_2^2} - m_2\right), h_0 = \left[\frac{n_2 Q\left(\beta + 2\sqrt{1 + m_2^2}\right)^{2/3}}{(\beta + m_2)^{5/3} i_2^{1/2}}\right]^{3/8}, b = \beta h_0$$

(28)

$$\beta = \frac{2}{\sqrt{1 + m_2^2}}, h_0 = 1.542\left[\frac{n_2 Q}{\sqrt{i_2}(2\theta_2 + 2m_2)}\right]^{3/8}, \theta_2$$

$$= \operatorname{atan}(1/m_2), R_2 = h_0, b = \beta h_0$$

(29)

where h_0 and β represent the normal water depth and width-depth ratio, respectively; b is the bottom width for a trapezoidal canal or the chord length of the arc-bottomed trapezoidal canal; R_2 and θ_2 denote the radius and radial angle of the arc bottom, respectively.

The heat, water, and mechanical parameters of the canal foundation soil are consistent with section 3.2.2. The elastic modulus and Poisson's ratio of concrete lining are 30 GPa and 0.2 respectively, with a density of 2500 kg/m³, thermal conductivity of 1.58 W/(m·K), and volumetric heat capacity of 2231 kJ/(m³·K). There are three arrangements of TLCGs for TLCGLS, including geomembrane-geomembrane contact (TLCGs with one-geotextile and one-geomembrane, Gmb-Gmb), geotextile-geomembrane contact (a layer composite geomembrane with one-geotextile and one-geomembrane and a layer composite geomembrane with two-geotextiles and one-geomembrane, Gmb-Gtt), and geotextile-geotextile contact (TLCGs with two geotextiles and one geomembrane, Gtt-Gtt). Their contact parameters are presented in Table 3 (Li et al.,

Table 3
Contact parameters between lining and frozen soil with TLCGs and NCG.

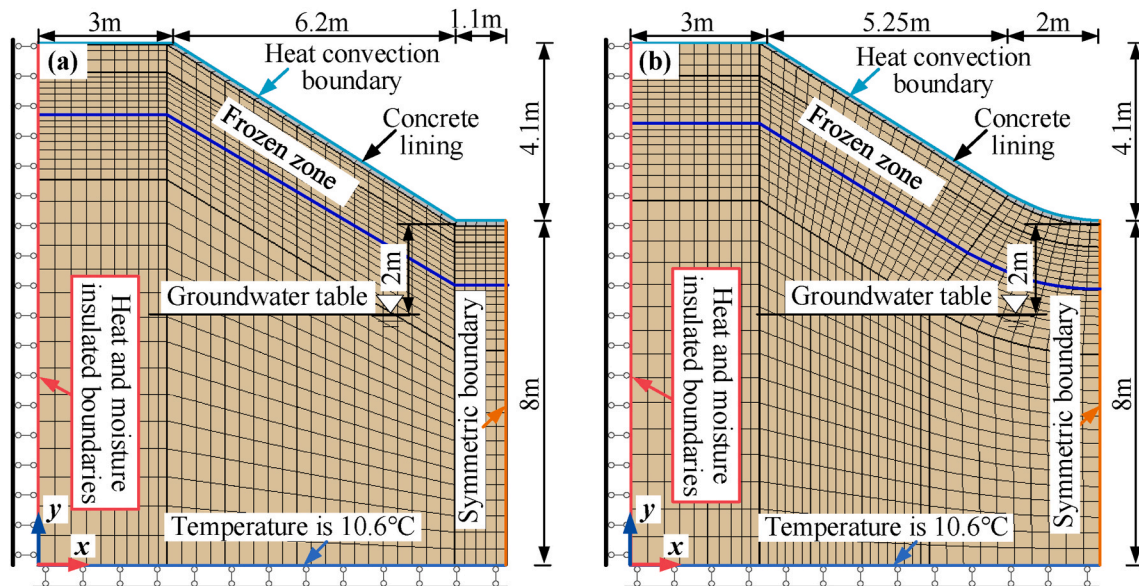| Forms	Shear stiffness (MPa/m)	Freezing strength (MPa)	Sliding friction coefficient
Gmb-Gmb	5.35	0.005	0.1
Gmb-Gtt	7.5	0.008	0.25
Gtt-Gtt	10	0.01	0.43
NCG	120	0.15	0.8

Fig. 16. Meshing, initial and boundary conditions of FE models: (a) trapezoidal canal; (b) arc-bottomed trapezoidal canal. The grid density in the frozen zone has been adjusted to a lower level for the purpose of observation.

2003; Wang et al., 2019).

The heat, water, and deformation boundaries of FE models are presented in Fig. 16. Based on the measured temperatures in Yinchuan City, Ningxia, an air temperature fitting equation with November 1st as an initial reference point is derived as follows:

$$T = 10.6 + 21.6 \sin\left(\frac{2\pi t}{365} + 3.48\right) \tag{30}$$

The canal has been constructed for many years, exhibiting a stable state in terms of temperature and deformation. Thus, the initial temperature field is established based on a stable temperature distribution influenced by air temperature (Eq. (30)), while the initial stress field is determined through static gravity calculations. The canal cuts off on October 15th, and the resulting water distribution serves as the initial water field. The calculation period spans from November 1st to March 30th of the subsequent year, with a maximum time step of 100s.

When there is no composite geomembrane in the canal, the interaction between the lining and frozen soil can be mathematically described using Eqs. (17), (18) and (20). However, considering the presence of normal freezing strength between the lining and frozen soil, Eq. (19) requires modification. The specific contact parameters are also provided in Table 3.

$$k_{An} = \begin{cases} E_s, \sigma_n < \tau_f \\ 0, \sigma_n \geq \tau_f \end{cases} \tag{31}$$

4.2. Effect of canal cross-sectional shapes

Taking the geotextile-geotextile contact (Gtt-Gtt) as an example, Fig. 17 shows the normal stress on the lining surface under the maximum freezing depth for both trapezoidal and arc-bottomed trapezoidal canals. The trapezoidal canal lining primarily experiences compressive forces, with some tensile stress observed at the center of its bottom. Both the maximum compressive stress and tensile stress surpass the concrete's design strength. For an arc-bottomed trapezoidal canal, it primarily undergoes compressive forces, exhibiting a gradual increase from the canal top to the slope toe, followed by a gradual decrease from the slope toe to the center of the canal bottom. Regrettably, the maximum compressive stress has surpassed the designated concrete's compressive strength. Following the installation of TLCGLS, there is a significant reduction in lining stress of the trapezoidal canal, with a maximum decrease of 22%. However, minimal changes are observed in the bottom lining's stress, particularly regarding tensile stress which exhibits a slight increasing trend. In addition, notable improvements are seen in the force exerted on the arc-bottomed trapezoidal canal's lining, with compressive stress decreasing by up to 31%. Therefore, considering the objective of reducing lining stress, TLCGLS is more suitable for arc-

bottomed trapezoidal canals.

Fig. 18 further shows the deformation trends for the trapezoidal and arc-bottom trapezoidal canals under NCG and Gtt-Gtt conditions at maximum freezing depth moment. Due to the canal's considerable depth, groundwater supply is limited, leading to frost heave mainly occurring near the canal bottom rather than its slopes. As shown in Fig. 18a and b, the sharp slope toe constrains soil frost heave at the trapezoidal canal's slope toe, while the interaction between the slope lining and bottom lining further reduces its deformation. After installing TLCGs, freezing constraints on the slope linings are alleviated, thereby reducing uplift forces exerted by the bottom lining. Consequently, this diminishes normal frost heave of the slope lining and subsequently reduces compressive stress on its lining. Simultaneously, the elevation of the slope toe reduces uneven deformation of the bottom lining. However, due to limitations of the sharp slope toe, releasing tangential deformation becomes challenging for the bottom lining, resulting in a slight reduction in stress and even an increase in tensile stress for a trapezoidal canal.

As shown in Fig. 18c and d, arc bottom section of the arc-bottomed trapezoidal canal exhibits a prominent uplift phenomenon. The arc slope toe facilitates a smooth transition of frost heave for the adjacent foundation soil, slope lining, and bottom lining without abrupt variations. After installing TLCGs, freezing constraint between the lining and frozen soil is significantly reduced, thereby decreasing the deformation constraint between the slope lining and bottom lining. Consequently, frost heaves in canal linings are released, effectively alleviating their frost heave stress. In addition, the relative tangential deformation between the lining of the arc-bottomed trapezoidal canal and frozen soil exhibits a significantly greater magnitude compared to that of the trapezoidal canal, thereby indicating that TLCGLS used in the arc-bottomed trapezoidal canal enhances its capacity to reduce freezing constraints and frost heave forces. Therefore, TLCGLS is deemed more suitable for application in arc-bottomed trapezoidal canals.

4.3. Effect of the arrangements of TLCGs

Taking the arc-bottomed trapezoidal canal as an example, four cases were designed: NCG, TLCGs with Gmb-Gmb, Gmb-Gtt, Gtt-Gtt. Fig. 19 shows the distributions of normal stress and deformation of the canal lining at the moment of maximum freezing depth for these cases. As shown in Fig. 19a, the transition from Gtt-Gtt to Gmb-Gtt to Gmb-Gmb results in a significant upward shift of the stress distribution curve, thereby leading to a noticeable reduction in compressive stress that gradually falls below the design compressive strength of concrete. However, tensile stress emerges at the center of the bottom lining and progressively exceeds the design tensile strength of concrete. By comparing the damaged zone sizes in canal linings, it can be found that
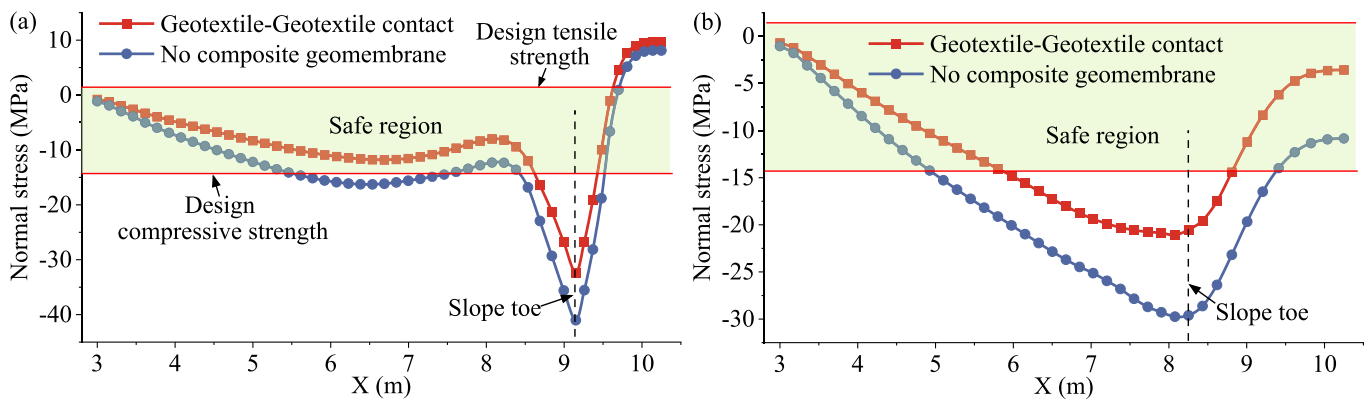

Fig. 17. Normal stress on the upper surface of the lining in cases involving Geotextile- Geotextile contact and no composite geomembrane at maximum freezing depth moment: (a) trapezoidal canal; (b) arc-bottomed trapezoidal canal. The canal lining constructed with C30 concrete exhibits a design tensile strength of 1.43 MPa and a design compressive strength of 14.3 MPa, respectively. This stress range is defined as the "Safe region" for the canal lining.
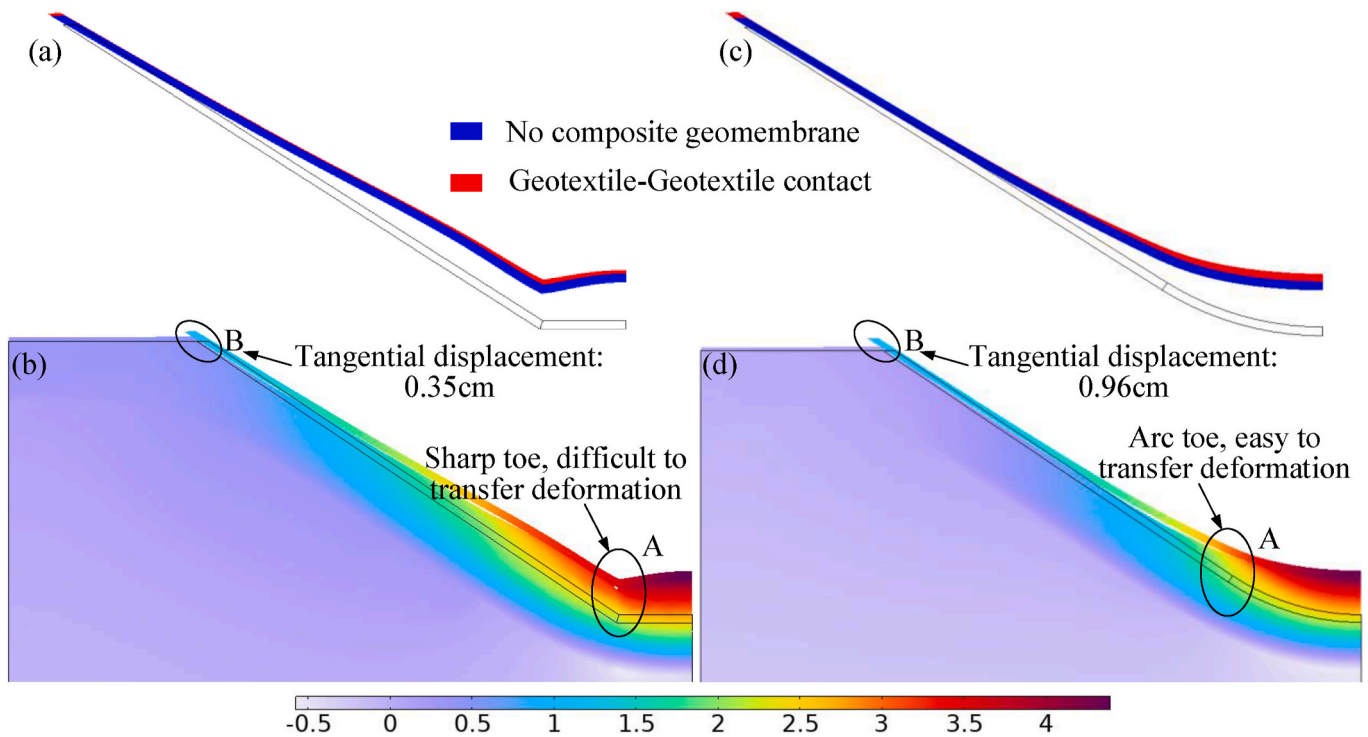
Fig. 18. Deformation trend diagram of the canal at maximum freezing depth moment (magnified by a factor of 15): (a) trapezoidal canal under NCG and Gtt-Gtt conditions; (b) trapezoidal canal under Gtt-Gtt condition; (c) arc-bottomed trapezoidal canal under NCG and Gtt-Gtt conditions; (d) arc-bottomed trapezoidal canal under Gtt-Gtt condition.
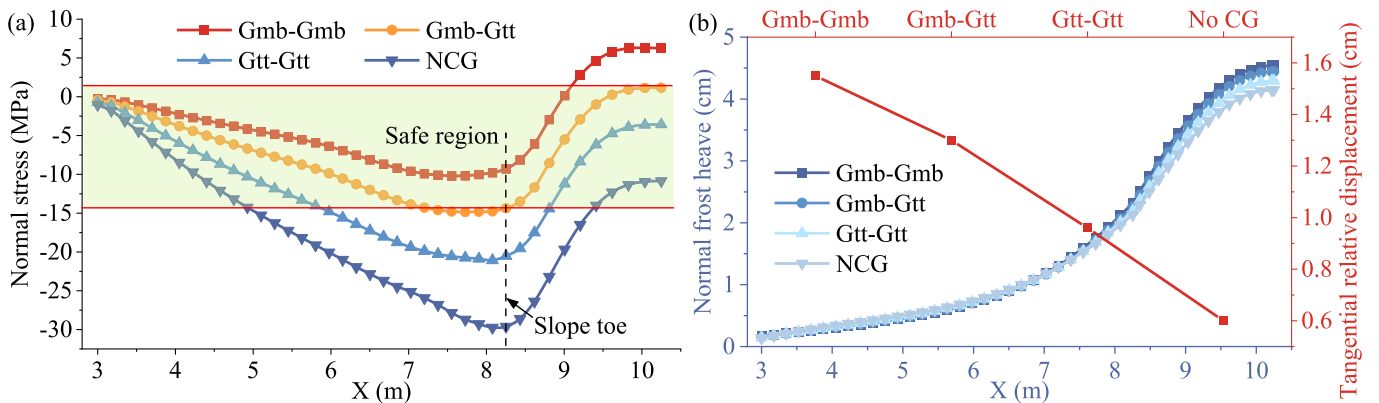

Fig. 19. Stress and displacement of the canal lining under different cases at maximum freezing depth moment: (a) normal stress; (b) normal and tangential relative displacement.

TLCGLS is an effective measure for mitigating frost damage in canals; however, improper utilization may lead to tensile failure at arc-bottom section. Based on the stress distribution of Gtt-Gtt, Gmb-Gtt, and Gmb-Gmb, it can be concluded that Gmb-Gtt yields the most favorable effect, which can maintain lining stress within a safe range while reducing frost heave stress by over 50%.

As shown in Fig. 19b, after installing TLCGs, the normal frost heave of the bottom lining increases significantly, while there is no significant change in frost heave of the slope lining. This is mainly because frost heave primarily occurs near the arc bottom. With the transition from Gtt-Gtt to Gmb-Gtt to Gmb-Gmb, there is an increase in normal frost heave of the bottom lining and a rise in relative tangential deformation between the lining and frozen soil. This observation suggests that reducing tangential freezing constraint can enhance tangential sliding between the lining and frozen soil, thereby alleviating normal frost heave of the lining. Ultimately, by adjusting internal forces within the

lining, it becomes possible to reduce frost heave stress.

4.4. Effect of the air temperature and soil type

Using the arc-bottomed trapezoidal canal under the Gmb-Gtt case as an example, further investigation was conducted to analyze the effect of air temperature and soil type on the anti-frost heave performance of TLCGLS, aiming to provide valuable insights for engineering applications in other regions. The average temperature (10.6 °C) is adjusted by increasing and decreasing it by 3 °C, based on Eq. (30), in order to analyze the effect of air temperature. By conducting sampling across multiple canals in the Ningxia region, the calculation parameters of soil-water characteristic curves and freezing curves for both silty clay and sandy soil were tested, thereby analyzing the effect of soil types. Specifically, for silty clay: $\theta_s = 0.39$, $\theta_r = 0.14$, $\alpha = 0.08$, $m = 0.38$, $k_s = 1.2 \times 10^{-8}$ m/s, $a = 9.1212$, $b = -0.3974$; for sandy soil: $\theta_s = 0.40$, $\theta_r = $
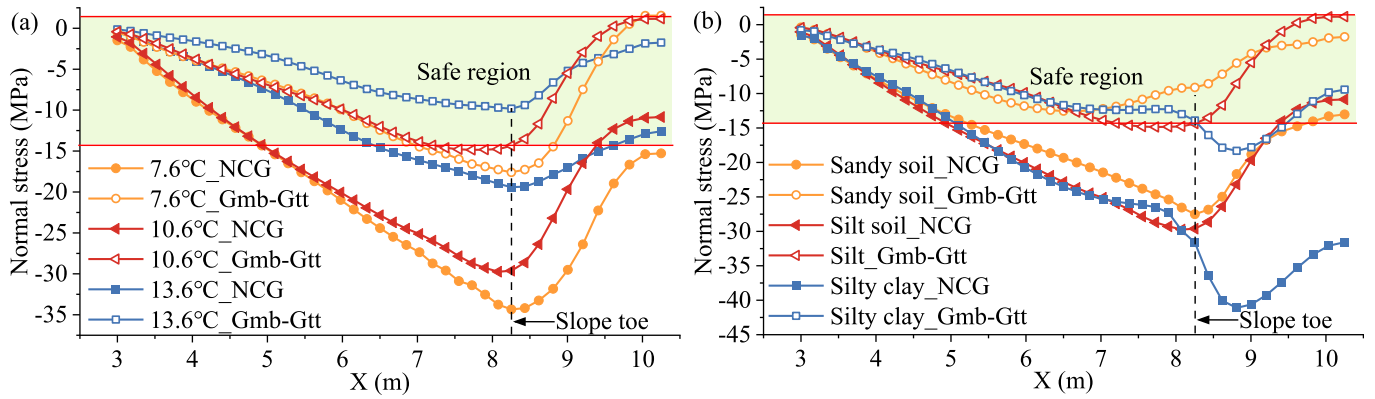
Fig. 20. Stress distribution of the canal lining under different air temperature and soil type at maximum freezing depth moment: (a) air temperature; (b) soil type.

0.05, $\alpha = 0.88$, $m = 0.33$, $k_s = 9.1 \times 10^{-7}$ m/s, $a = 5.5734$, $b = -0.4651$.

Fig. 20 shows the distributions of normal stress of the canal lining at the moment of maximum freezing depth for these cases. As shown in Fig. 20, a decrease in air temperature and the transition from sandy soil to silt to silty clay result in a progressive increase in frost heave strength of canal foundation soil. Consequently, this leads to an escalating pressure stress on the canal lining that exceeds the designed compressive strength of concrete. After installing TLCGLS, there is a rapid reduction in pressure stress on the canal lining, gradually approaching a safe region. Combined with Fig. 19a, it is evident that the maximum stress reduction surpasses 50% with Gmb-Gtt while effectively controlling the tensile stress within a safe range. Therefore, Gmb-Gtt configuration remains as the optimal choice. Furthermore, as lining pressure increases, the stress reduction effect of TLCGLS gradually intensifies.

4.5. Anti-frost heave mechanism

To investigate the anti-frost heave mechanism of TLCGLS, Fig. 21a and b depict the canal frost heave trends under two cases of NCG and Gmb-Gtt. In the case of NCG (Fig. 21a), due to the strong freezing constraint between the lining and frozen soil, the substantial upward displacement of the bottom lining exerts a significant jacking on the slope lining, thereby causing its compressive stress to exceed the design compressive strength of concrete. The slope lining also restricts the upward deformation of the bottom lining, resulting in a significant increase in jacking force on the bottom lining. This reduces frost heave of the bottom lining but results in elevated compressive stress that surpass the design compressive strength of concrete.

In the case of Gmb-Gtt (Fig. 21b), the freezing constraints between the lining and frozen soil are significantly reduced, resulting in a

decrease in mutual constraint between the bottom lining and slope lining. This mitigates the jacking force at the slope toe, leading to a substantial decrease in compressive stress on the slope lining. In addition, the reduced jacking force also decreases the constraint on the bottom lining, facilitating normal frost heave release and alleviating lining compressive stress. Combined with Fig. 19, with the transition from Gtt-Gtt to Gmb-Gtt to Gmb-Gmb, the friction coefficient between TLCGs gradually decreases and consequently leads to a decrease in lining compressive stress. However, tensile stress arises at the center of the bottom lining due to attenuation of arching effect in the arc bottom lining.

Based on the stress and deformation characteristics of the canal lining, the anti-frost heave mechanism diagram for TLCGLS is presented in Fig. 21c. The lining structure can be conceptualized into models: the slope toe acts as a fixed support, the arc bottom lining is simplified as an arch with fixed supports at slope toes, and the slope lining is simplified as a hyperstatic beam with a fixed support at the slope toe and simply supported at the top. The lining is subjected to active forces, such as normal and tangential frost heave forces, as well as passive forces like tangential freezing forces, in addition to a jacking force exerted at the slope toe. The decrease in the friction coefficient between the lining and frozen soil leads to a reduced freezing constraint, resulting an increased tangential displacement at both fixed and simply supports of the slope lining. Consequently, this mitigates compressive stress caused by bottom lining jacking and frost heave on the slope. Meanwhile, the decrease in jacking force at the slope toe enhances displacements in fixed supports of the arch bottom lining, leading to a gradual decrease in height and weakening of the arching effect. As a result, this releases the normal frost have of the bottom lining, leading to a reduction in its compressive stress. However, it also reduces both stiffness and bearing capacity of the
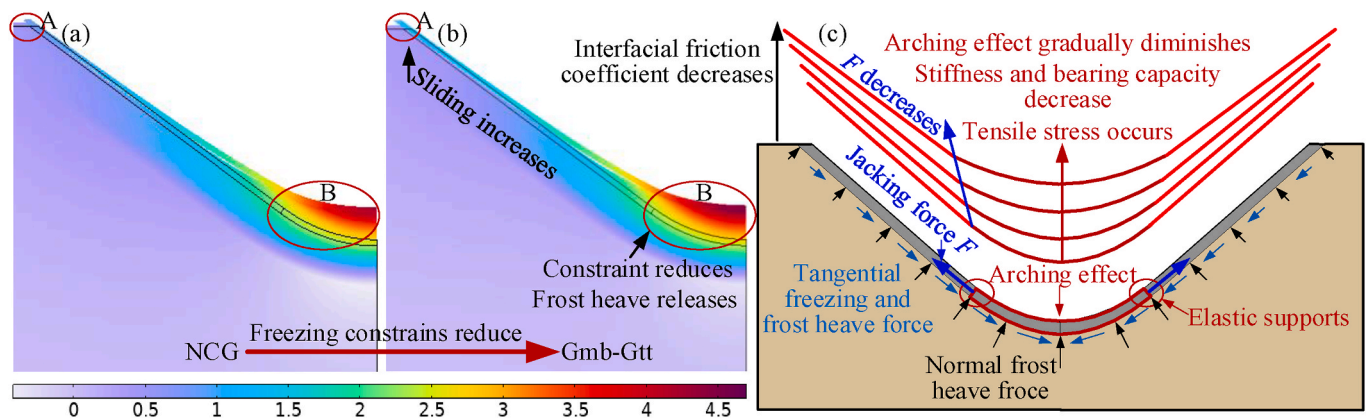

Fig. 21. Deformations and frost heave reduction mechanism of TLCGLS: (a) Gmb-Gtt at maximum freezing depth moment; (b) NCG at maximum freezing depth moment; (c) schematic diagram of the frost heave reduction mechanism.

arc bottom lining, progressively causing tensile stress failure. Therefore, the appropriate arrangement of TLCGs can effectively mitigate freezing constraints between the lining and frozen soil, allowing for controlled tangential sliding between them to accommodate normal frost heave of the lining. TLCGLS with Gmb-Gtt configuration can fully exploit the arching effect of the bottom lining to reduce compressive stress while ensuring that tensile stress meets design requirements, thereby enhancing the frost heave adaptability of canal linings. This is the mechanism why Gmb-Gtt configuration exhibits superior effectiveness.

The key to TLCGLS lies in minimizing compressive stress on the lining while ensuring that tensile stress remains within the designed tensile strength of concrete. When the stress on the lining significantly exceeds its capacity, TLCGLS can only mitigate the extent of damage to the lining, while cracks may still occur. In such cases, additional measures should be employed to further minimize frost damage. Considering that a composite geomembrane exhibits a substantially higher elongation at break (60%) compared to canal deformation caused by soil frost heave, failure is unlikely to occur. Moreover, this composite geomembrane demonstrates exceptional resistance against chemical corrosion and aging due to its long-term burial beneath concrete lining which ensures minimal impact from external environmental factors. Furthermore, TLCGs establish contact with both the soil and the lining through geotextiles, effectively safeguarding the interface between TLCGs and geomembranes, thereby enhancing their impermeability and long-term durability. TLCGs are crucial components of TLCGLS for frost damage prevention. The cracks in the lining have minimal impact on the anti-frost heave performance of TLCGLS, and prompt repair of surface cracks can restore its anti-frost heave capabilities. Therefore, TLCGLS exhibit exceptional long-term durability and possess immense potential for on-site engineering applications.

Based on the anti-frost heave mechanism of an arch-bottomed trapezoidal canal with TLCGLS, the following valuable insights can be derived:

(1) The arch configuration of the bottom lining significantly influences the arrangements of TLCGs. When designing canal cross-sections, the main consideration is water conveyance capacity, which can be achieved through either the hydraulic optimal section or the practical economic section (Jiang et al., 2022b). The hydraulic optimal section is typically narrow and deep, imposing significant constraints on the tangential sliding between the lining and frozen soil. In such cases, it is recommended to reduce frost damage by using Gmb-Gtt arrangement proposed in this study. On the other hand, the practical economic section of the canal is wide and shallow, reducing constraints on tangential sliding capacity between the lining and frozen soil. Therefore, it is advisable to use a higher friction force that allows for appropriate sliding between them, such as through either Gmb-Gtt or Gtt-Gtt arrangements.

(2) The appropriate friction between TLCGs plays a crucial role in mitigating canal frost damage. This study integrates the currently available composite geomembranes (one-geotextile and one-geomembrane; two-geotextiles and one-geomembrane) in the market, proposing three arrangements for TLCGs. According to the results from this study (Fig. 19), optimal performance of the slope lining can be achieved by minimizing friction forces between TLCGs, thus selecting Gmb-Gmb. For the bottom lining, reducing friction between TLCGs leads to a decrease in compressive stress but an increase in tensile stress. Therefore, in addition to adopting Gmb-Gmb arrangement (consistent with the slope), incorporating anti-slip materials on the geomembrane can be considered to enhance interface friction on the bottom lining. By strategically adjusting their positions and sizes, it is possible to further optimize the lining stress to meet the design requirement, thereby enhancing anti-frost heave performance. This structure or TLCGs can be pre-processed in the factory based on the canal

dimension and then assembled on-site. The construction procedure aligns with that of one-layer composite geomembrane without complicating the construction process.

5. Conclusions

From the perspective of reducing the freezing force between canal lining and frozen soil, TLCGLS is proposed to mitigate canal frost damage. Firstly, model tests were conducted to investigate the heat-water transfer and stress-deformation responses of canals with and without TLCGLS. The test results have been meticulously compared to previous data, ensuring their reasonability and reliability. Secondly, a canal frost heave model with heat-water-mechanical coupling was developed to account for the interaction among canal lining, TLCGs, and frozen soil. Thirdly, the influence of canal cross-section shapes and arrangements of TLCGs on the anti-frost heave performance of TLCGLS were investigated, and its anti-frost heave mechanism was revealed. The main conclusions are as follows:

(1) The freezing rate of the canal follows the order: bottom < slope < top, resulting in a corresponding water migration amount: bottom > slope > top, thereby inducing canal frost heave as: bottom > slope > top.

(2) TLCGLS increase the relative tangential deformation between canal lining and foundation soil, resulting in a reduction of 35% in uneven frost heave of the lining. In addition, it mitigates compressive strains by 29% and tensile strains by 28% in the lining. During the melting process, TLCGLS can rapidly reduce frost heave, strain, and relative tangential deformation, as well as residual deformation and residual strain, exhibiting a robust resetting ability. Therefore, TLCGLS has a pronounced anti-frost heave effect.

(3) The nonlinear contact model in the canal frost heave model is based on elastic thin layer elements, ensuring accurate calculations and enhancing model convergence. The model was then validated by tests, providing a feasible method for a rapid design for TLCGLS.

(4) TLCGLS lead to a 22% reduction in slope lining stress and negligible stress reduction in bottom lining of trapezoidal canals. Moreover, it effectively mitigates freezing constraints between the lining and frozen soil, resulting in a significant 31% reduction in lining stress for arc-bottomed trapezoidal canals. Therefore, TLCGLS is more suitable for arc-bottomed trapezoidal canals.

(5) The arc bottom lining is simplified as an arch with fixed supports at slope toes, while the slope lining is simplified as a hyperstatic beam with a fixed support at the slope toe and simply support at the canal top. The decrease in friction between TLCGs increases the tangential deformation at the supports, diminishing the arching effect of the bottom lining. This diminishes its compressive stress but induces tensile stress, which poses a threat to structural safety.

(6) TLCGLS with Gmb-Gtt exhibits superior anti-frost heave effect, effectively optimizing the utilization of arching effect in the arc bottom lining and releasing its frost heave. This results in a significant reduction in compressive stress while ensuring that tensile stress meets design requirements, ultimately reducing lining stress by over 50%.

The canal primarily frost heaves at the bottom section in numerical case. However, canals with shallow groundwater table also frost heaves significantly on the slope. Further investigation is needed to assess the anti-frost heave performance of TLCGLS under such circumstances.

CRediT authorship contribution statement

Haoyuan Jiang: Writing – original draft, Methodology, Funding

acquisition, Data curation. **Mingyi Zhang:** Writing – review & editing, Supervision, Funding acquisition. **Zhengzhong Wang:** Writing – review & editing, Conceptualization. **Yi Wang:** Validation, Methodology, Data curation. **Zhengyi Wang:** Validation, Formal analysis, Data curation. **Xinjian Sun:** Validation, Formal analysis.

Declaration of competing interest

The authors declare that they have no known competing financial interests or personal relationships that could have appeared to influence the work reported in this paper.

Acknowledgements

Data availability

Data will be made available on request.

References

Arzanfudi, M.M., Al-Khoury, R., Sluys, L.J., Schreppers, G.M.A., 2020. A thermo-hydro-mechanical model for energy piles under cyclic thermal loading. Comput. Geotech. 125, 103560. https://doi.org/10.1016/j.compgeo.2020.103560.

Bai, R.Q., Lai, Y.M., Pei, W.S., Zhang, M.Y., 2020. Investigation on frost heave of saturated–unsaturated soils. Acta Geotech. 15, 3295–3306. https://doi.org/10.1007/s11440-020-00952-6.

Berdugo, M., Delgado-Baquerizo, M., Soliveres, S., et al., 2020. Global ecosystem thresholds driven by aridity. Science 367, 787–790. https://doi.org/10.1126/science.aay5958.

Chen, P.P., Qi, L.H., Zhang, X.B., Ma, L., Yang, G.G., Qi, J.L., 2023. Analysis of heat–moisture coupling transfer for unsaturated soil under freezing and thawing based on fractal theory. Cold Reg. Sci. Technol. 206, 103744. https://doi.org/10.1016/j.coldregions.2022.103744.

Chen, Y., Huang, Y.H., Cai, Z.Y., Su, A.S., 2023. Failure mechanism and treatment measures for expansive soil canals in cold regions: a case study of the Xinjiang Water Conveyance Canal in China. Cold Reg. Sci. Technol. 216, 103991. https://doi.org/10.1016/j.coldregions.2023.103991.

FAO, 2021. The state of the world's land and water resources for food and agriculture – systems at breaking point. Synthesis report 2021. Rome. https://doi.org/10.4060/cb7654en.

Faúndez, M., Alcayaga, H., Walters, J., Pizarro, A., Soto-Alvarez, M., 2023. Sustainability of water transfer projects: a systematic review. Sci. Total Environ. 860, 160500. https://doi.org/10.1016/j.scitotenv.2022.160500.

Gao, Y.Y., Chen, J., Qian, H., Wang, H.K., Ren, W.H., Qu, W.G., 2022. Hydrogeochemical characteristics and processes of groundwater in an over 2260year irrigation district: a comparison between irrigated and nonirrigated areas. J. Hydrol. 606, 127437. https://doi.org/10.1016/j.jhydrol.2022.127437.

Guo, Y., Shen, Y.J., 2016. Agricultural water supply/demand changes under projected future climate change in the arid region of northwestern China. J. Hydrol. 540, 257–273. https://doi.org/10.1016/j.jhydrol.2016.06.033.

Haj-Amor, Z., Araya, T., Kim, D.G., Bouri, S., Lee, J., Ghiloufi, W., Yang, Y.R., Kang, H., Jhariya, M.K., Banerjee, A., Lal, R., 2022. Soil salinity and its associated effects on soil microorganisms, greenhouse gas emissions, crop yield, biodiversity and desertification: a review. Sci. Total Environ. 843, 156946. https://doi.org/10.1016/j.scitotenv.2022.156946.

Hao, X.Y., Ma, W., Feng, W.J., Wen, Z., Zhang, L.H., Chen, S.J., 2023. Investigation on the frost heave-induced pressure and hydro-thermal processes in freezing soil under rigid constraint and hydraulic pressure. Eng. Geol. 323, 107238. https://doi.org/10.1016/j.enggeo.2023.107238.

Harlan, R.L., 1973. Analysis of coupled heat-fluid transport in partially frozen soil. Water Resour. Res. 9 (5), 1314–1323. https://doi.org/10.1029/WR009i005p01314.

Heibaum, M., 2014. Geosynthetics for waterways and flood protection structures — controlling the interaction of water and soil. Geotext. Geomembranes 42, 374–393. https://doi.org/10.1016/j.geotexmem.2014.06.003.

Jiang, H.Y., Gong, J.W., Wang, Z.Z., et al., 2022a. Analytical solution for the response of lined trapezoidal canals under soil frost action. Appl. Math. Model. 107, 815–833. https://doi.org/10.1016/j.apm.2022.03.016.

Jiang, H.Y., Li, L.X., Wang, Z.Z., Gong, J.W., Sun, T., Li, H.X., 2022b. Anti-frost heave design method for a parabolic canal based on the hydraulic optimal solution set in seasonally frozen regions. Cold Reg. Sci. Technol. 193, 103433. https://doi.org/10.1016/j.coldregions.2021.103433.

Jiang, H.Y., Liu, Q.H., Wang, Z.Z., Gong, J.W., Li, L.X., 2022c. Frost heave modelling of the sunny-shady slope effect with moisture-heat-mechanical coupling considering solar radiation. Sol. Energy 233 (11), 292–308. https://doi.org/10.1016/j.solener.2022.01.040.

Jiang, H.Y., Wang, Z.Z., Wang, Y., Liu, Q.H., Ge, J.R., 2019. Study on anti-frost heave mechanism and application of "reasonable joints" for large-size trapezoidal canal with arc-bottom. J. Hydraul. Eng. 50, 947–959. https://doi.org/10.13243/j.cnki.slxb.20190299.

Li, Q., Sun, S.F., Xue, Y.K., 2010. Analyses and development of a hierarchy of frozen soil models for cold region study. J. Geophys. Res. Atmos. 115, D03107. https://doi.org/10.1029/2009JD012530.

Li, S.Y., Wang, C., Yang, J.L., Lai, Y.M., Qi, J., Wan, X.S., 2022. Thermo-hydro-mechanical process and damage mechanism of a cold-region canal under coupled wetting-drying and freezing-thawing cycles. Acta Geotech. 17, 4655–4665. https://doi.org/10.1007/s11440-022-01531-7.

Li, Y., Chen, D.C., Jin, Y., 2003. Friction characteristics of geotextile. J. Northeast For. Univ. (2), 67–69.

Li, Z., Liu, X.Y., Sun, Y., Jiang, X., 2024. Numerical simulation of frost heaving damage of earth-rock dam berms in cold regions with thermo-hydro-mechanical coupling. Cold Reg. Sci. Technol. 223, 104207. https://doi.org/10.1016/j.coldregions.2024.104207.

Liu, D.H., Zheng, H., 2023. Numerical simulation of frost heaving damage of earth-rock dam berms in cold regions with thermo-hydro-mechanical coupling. Appl. Therm. Eng. 233, 121042. https://doi.org/10.1016/j.applthermaleng.2023.121042.

Liu, H.L., Ma, D.H., Wang, C.M., Liu, X.Y., Wu, D., Khan, K.U.J., 2021. Study on the frost heave mechanism of the water conveyance canal and optimized design of slope protection. Bull. Eng. Geol. Environ. https://doi.org/10.1007/s10064-021-02447-4.

Liu, J.K., Wang, T.F., Tai, B.W., Lv, P., 2020. A method for frost jacking prediction of single pile in permafrost. Acta Geotech. 15, 455–470. https://doi.org/10.1007/s11440-018-0711-0.

Liu, Q.H., Wang, Z.Z., Li, Z.C., Wang, Y., 2020. Transversely isotropic frost heave modeling with heat–moisture–deformation coupling. Acta Geotech. 15, 1273–1287. https://doi.org/10.1007/s11440-019-00774-1.

Mao, D.H., Wang, Z.M., Wu, B.F., Zeng, Y., Luo, L., Zhang, B., 2018. Land degradation and restoration in the arid and semiarid zones of China: quantified evidence and implications from satellites. Land Degrad. Dev. 29, 3841–3851. https://doi.org/10.1002/ldr.3135.

Ming, F., Zhang, M.Y., Pei, W.S., Chen, L., 2023. Correction of the thermal conductivity of polyurethane insulation material under freeze-thaw and water absorption conditions and its application. Cold Reg. Sci. Technol. 211, 103859. https://doi.org/10.1016/j.coldregions.2023.103859.

Muluti, S.S., Kalumba, D., Sobhee-Beetul, L., Chebet, F., 2023. Shear strength of single and multi-layer soil–geosynthetic and geosynthetic–geosynthetic interfaces using large direct shear testing. Int. J. Geosynth Groun 9, 33. https://doi.org/10.1007/s40891-023-00450-1.

Pan, R.K., Yang, P., Yang, Z.H., 2022. Experimental study on the shear behavior of frozen cemented sand-structure interface. Cold Reg. Sci. Technol. 197, 103516. https://doi.org/10.1016/j.coldregions.2022.103516.

Scanlon, B.R., Fakhreddine, S., Rateb, A., et al., 2023. Global water resources and the role of groundwater in a resilient water future. Nat. Rev. Earth Environ. 4, 87–101. https://doi.org/10.1038/s43017-022-00378-6.

Shao, H.H., Xu, H.H., Zhu, W.S., Wu, H., Liu, Z.Q., 2023. Thermal-mechanical properties of polystyrene insulation board under defect condition and their influence on lining structure of conveyance channel. Cold Reg. Sci. Technol. 206, 103752. https://doi.org/10.1016/j.coldregions.2022.103752.

Shi, J.Y., Shu, S., Qian, X.D., Wang, Y.C., 2020. Shear strength of landfill liner interface in the case of varying normal stress. Geotext. Geomembranes 48, 713–723. https://doi.org/10.1016/j.geotexmem.2020.05.004.

Shi, L.H., Li, S.Y., Wang, C., Yang, J.L., Zhao, Y.C., 2023. Heat-moisture-deformation coupled processes of a canal with a berm in seasonally frozen regions. Cold Reg. Sci. Technol. 207, 103773. https://doi.org/10.1016/j.coldregions.2023.103773.

Teng, J.D., Liu, J.L., Zhang, S., Sheng, D.C., 2023. Frost heave in coarse-grained soils: experimental evidence and numerical modelling. Geotechnique 73, 1100–1111. https://doi.org/10.1680/jgeot.21.00182.

Tian, Y.H., Yang, Z.H., Tai, B.W., Li, Y.L., Shen, Y.P., 2019. Damage and mitigation of railway embankment drainage trench in warm permafrost: a case study. Eng. Geol. 261, 105276. https://doi.org/10.1016/j.enggeo.2019.105276.

Wang, Y., Wang, Z.Z., Liu, Q.H., Liu, Y., 2019. Double membranes cushion layout for preventing frost heave damage based on elastic thin contact model. Trans. Chin. Soc. Agric. Eng. 35, 133–141. https://doi.org/10.11975/j.issn.1002-6819.2019.12.016.

Wang, Z.X., Cao, C., Yu, Q.B., Wang, Q., Niu, C.C., Shen, J.J., Zhu, K.X., Liu, J., Han, M. X., Fu, H.C., Sun, X., Xia, W.T., Sun, D., Shu, H., Ji, Y.P., Xue, J.Y., Shan, X.H., 2024. Multi-scale failure mechanisms of hydraulic engineering exposed to seasonally frozen salinization environment: integrating SBAS-InSAR and mechanical experiments. Sci. Total Environ. 912, 169210. https://doi.org/10.1016/j.scitotenv.2023.169210.

Wang, Z.Z., 2004. Establishment and application of mechanics models of frost heaving damage of concrete lining trapezoidal open canal. Trans. Chin. Soc. Agric. Eng. 20, 24–29.

World Economic Forum, 2020. The Global Risks Report 2020, fourteenth ed. World Economic Forum, Geneva https://www.weforum.org/reports/the-global-risks-report-2020.

Xu, G.J., Shi, J.Y., Li, Y., 2023. Change pattern of geomembrane surface roughness for geotextile/textured geomembrane interfaces. Geotext. Geomembranes 51, 88–99. https://doi.org/10.1016/j.geotexmem.2022.09.009.

Yu, W.B., Zhang, T.Q., Lu, Y., Han, F.L., Zhou, Y.F., Hu, D., 2020. Engineering risk analysis in cold regions: state of the art and perspectives. Cold Reg. Sci. Technol. 171, 102963. https://doi.org/10.1016/j.coldregions.2019.102963.

Zhang, M.Y., Lu, J.G., Pei, W.S., Lai, Y.M., Yan, Z.R., Wan, X.S., 2021. Laboratory study on the frost-proof performance of a novel embankment dam in seasonally frozen regions. J. Hydrol. 602, 126769. https://doi.org/10.1016/j.jhydrol.2021.126769.

Zhang, Z.X., Kushwaha, R.L., 1998. Modeling soil freeze-thaw and ice effect on canal bank. Can. Geotech. J. 35, 655–665.

Zhu, R., Cai, Z.Y., Huang, Y.H., Zhang, C., Guo, W.L., Zhu, X., 2021. Centrifugal and field studies on water infiltration characteristics below canals under wetting-drying-freezing-thawing cycles. J. Cent South Univ. 28, 1519–1533. https://doi.org/10.1007/s11771-021-4703-0.